Revised manuscript submitted to Materials Science and Engineering A (September 2023)

Flow behaviour and microstructural stability in an Al-3Mg-0.2Sc alloy processed by high-pressure torsion at different temperatures

Pedro Henrique R. Pereira [a,*], Piotr Bazarnik [b], Yi Huang [c,d], Malgorzata Lewandowska [b] and Terence G. Langdon [c]

[a]Department of Metallurgical and Materials Engineering, Universidade Federal de Minas Gerais, Belo Horizonte 31270-901, MG, Brazil.

[b]Faculty of Materials Science and Engineering, Warsaw University of Technology, Woloska 141, 02-507 Warsaw, Poland.

[c]Materials Research Group, Department of Mechanical Engineering, University of Southampton, Southampton SO17 1BJ, U.K.

[d]Department of Design and Engineering, Faculty of Science and Technology, Bournemouth University, Poole, Dorset BH12 5BB, U.K.

Abstract

Experiments were performed to examine the flow behaviour at room temperature (RT ≈ 300 K) and the microstructural stability of a solution-treated Al-3Mg-0.2Sc alloy processed through 10 turns of high-pressure torsion (HPT) at either RT or 450 K and further annealed for 1 h at temperatures (T) up to 773 K. The results revealed that the Al-3Mg-0.2Sc alloy achieved yield strengths of ~590 and 540 MPa after HPT at RT and 450 K, respectively. This followed from the higher dislocation densities achieved after processing at RT since both microstructures had average grain diameters of ~320 nm. After annealing at $T \geq 523$ K, there was evidence for the onset of dynamic strain ageing (DSA) during tensile testing at RT and this occurred concurrently with increases in the elongations to failure. The grain structures developed during HPT at 450 K exhibited superior microstructural stability than after HPT at RT for comparable heating conditions. A model derived for materials having second-phase particles was applied to understand the microstructural evolution observed during heating. It is shown that the values calculated for the driving and restraining pressures for boundary migration and the boundary stability factors are consistent with the experimental results.

Keywords: Aluminium alloys; Grain refinement; Flow properties; High-pressure torsion; Microstructural stability; Portevin-Le Chatelier effect.

*Corresponding author: Pedro Henrique R. Pereira (ppereira@demet.ufmg.br)

1. Introduction

The need for more fuel-efficient transports has driven the tailoring of novel aluminium alloys with high load bearing capacities and low densities [1–4]. Some applications such as aircraft also demand resistance against incipient recrystallisation after exposure at high temperatures for short periods of time. This can be achieved by the addition of dispersoid-forming elements such as Zr, Ce, and Sc in the Al alloys [5–7]. Al-Mg-Sc alloys with up to 0.3 wt.% Sc are capable of significantly delaying recrystallisation due to the formation of nano-sized Al_3Sc dispersoids [7–10]. These precipitates hinder grain boundary migration due to the Zenner pinning effect which enhances the microstructural stability by comparison with alloys having no second phases [11–13].

The superior thermal stability of Al-Mg-Sc alloys is especially appealing considering the possibility of retaining ultrafine-grained (UFG) structures produced by severe plastic deformation (SPD) procedures [14,15], such as equal-channel angular pressing (ECAP) [16] and high-pressure torsion (HPT) [17,18], after heating for prolonged times. As recently reported [19,20], the presence of Al_3Sc makes it possible to achieve extremely high elongations to failure in SPD-processed Al-Mg-Sc alloys due to deformation through grain boundary sliding [21–23]. It is noted, however, that the Al-3Mg-0.2Sc alloy has finer grain sizes after HPT [24–26] but it exhibits lower superplastic ductilities than after ECAP due to the occurrence of grain coarsening during deformation at high homologous temperatures (T_H) [19,24,27,28].

These results have motivated several investigations which were designed to evaluate procedures for further improving the thermal stability of nanostructured materials. Some of these strategies include inducing the formation of nanosized particles and/or solute segregation at grain boundaries by applying the SPD procedure in alloys having second phase particles prior to processing [29–34] and the processing of alloys at higher temperatures [26,35–37]. It was shown that the Al-3Mg-0.2Sc alloy achieves an

elongation to failure of ~1020 % during testing at 523 K and at 10^{-3} s^{-1} after HPT at 450 K [26]. On the other hand, the same metal after HPT at RT reaches an elongation of ~620 % when tested under an equivalent condition. These differing results demonstrate the need for conducting a more thorough investigation to model the microstructural changes in HPT-processed Al-Mg-Sc alloys during heating at various temperatures.

Although different studies have examined the flow behaviour of Al-Mg-Sc alloys after processing by ECAP or other conventional metal-working techniques [38–40], there is a lack of data on the flow properties at room temperature (RT) for this alloy after processing by HPT. In addition, if annealing is undertaken after processing, the onset of different solid-state reactions such as static recovery and precipitation could offer conditions for the achievement of an adequate combination between material strength and ductility and thereby provide important insight on the tailoring of the mechanical properties of this alloy.

Accordingly, the current research was designed to study the effect of HPT processing at different temperatures on the flow behaviour at ambient temperature and the microstructural stability of an Al-3Mg-0.2Sc alloy processed by HPT at either RT or 450 K and with subsequent annealing for 1 h at temperatures up to 773 K. A theoretical model was used to provide further understanding on the microstructural changes observed in the HPT-processed alloy during heating.

2. Experimental material and procedures

This investigation was undertaken using Al-3% Mg-0.2% Sc (% in weight) billets of ~10 mm diameter provided by the China Rare Metal Material Corporation in the as-forged state. First, the as-received Al-Mg-Sc billets were solution-treated at 880 ± 2 K for 1 h and thereafter quenched in iced water to homogenise the grain structures and maximise the Sc content in the Al matrix. The solubilised bars were cut in the form of discs having thicknesses of ~1 mm and thereafter were ground down to ~0.8 mm.

The solution-treated Al-Mg-Sc discs were processed through quasi-constrained HPT [41,42] at either room temperature (~300 K) or at 450 ± 5 K. The high temperature was achieved by using a resistive heating element positioned around the anvils as described in earlier investigations [29,35,43]. First, the discs were compressed within the shallow depression of the anvils [44] using a nominal pressure of 6 GPa. For processing at ~450 K the pressure was held constant without any rotation of the lower anvil for ~10 min to permit a more accurate temperature control and thereafter the discs were subjected to 10 revolutions at a rotation speed of ~1 rpm.

Afterwards, the HPT-processed discs were annealed for 1 h at selected temperatures from 423 to 773 K. For each procedure, the furnace was heated to the annealing temperature and then the HPT-processed discs were rapidly inserted into the hot chamber to give a nearly isothermal heating condition.

The flow behaviours of the Al-3Mg-0.2Sc alloy processed by up to 10 turns of HPT followed by annealing at different conditions were assessed through tensile testing using miniature specimens with gauge lengths and widths of ~1.1 and 1.0 mm, respectively. As in earlier reports [29,45–47], two off-centre specimens were cut from each processed disc using electrical discharge machining. The surfaces of the tensile specimens were carefully flattened through grinding and polishing down to ~0.6 mm to remove any irregularities impressed by the anvils during processing. Tensile tests were carried out at RT using a Zwick Z030 universal testing machine at a constant rate of crosshead displacement to give an initial strain rate of 1.0×10^{-3} s^{-1}.

The microstructures of the HPT-processed and subsequently annealed Al-Mg-Sc discs were examined through orientation imaging microscopy using electron backscattered diffraction (EBSD). Sample preparation involved grinding using abrasive papers and final polishing using 0.06 μm silica colloidal. EBSD scans were conducted at positions located at ~3 mm from the disc centres using a JSM6500F thermal field

emission microscope with a minimum step size of 30 nm. Orientation maps were generated from each EBSD scan and these results were used to calculate the area-weighted grain diameters and assess the distributions of the correlated misorientation angles and the grain diameters.

The Al-3Mg-0.2Sc alloy was also examined through transmission electron microscopy (TEM) using a JEOL 1200EX facility. Discs of ~3 mm in diameter were punched at positions located at ~3.5 mm from the centre of both the HPT-processed discs and the discs subjected to post-HPT annealing for 1 h at 673 K. The punched discs were electropolished using a Struers Tenupol-5 system using an electrolytic solution of 30% HNO_3 and 70% CH_3OH at ~250 K.

The surfaces of the HPT-processed discs were analysed by means of X-Ray diffraction (XRD) using a Bruker D2 Phaser X-ray diffractometer with Cu Kα radiation. The XRD profiles were recorded through θ-2θ scans undertaken with a step size of 0.02° and using a scanning angle interval from 30 to 110°. The mean crystallite size (D_c) and the microstrain ($\langle \varepsilon^2 \rangle^{1/2}$) were estimated from Maud software and these parameters were used to estimate the density of dislocations (ρ) from the following expression [48,49]:

$$\rho = \frac{2\sqrt{3}\,\langle \varepsilon^2 \rangle^{1/2}}{D_c\,\mathbf{b}} \quad (1)$$

where $\mathbf{b}$ is the modulus of the Burgers vector.

3. Experimental Results

3.1 Tensile properties

Fig. 1 shows engineering stress vs engineering strain curves obtained at RT for the Al-3Mg-0.2Sc alloy after 10 turns of HPT at either 300 or 450 K and subsequently annealed for 1 h at temperatures ranging from 423 to 773 K. It is readily apparent that the material exhibits extremely high flow stresses, exceeding 650 MPa, immediately after

HPT at RT. Nevertheless, it displays very limited ductility such that the material fails without any noticeable necking.

After annealing at increasing temperatures, the stress-strain curves of the alloy processed at RT show a clear trend of increasing ductility and a reduction in the flow stresses during tensile testing. Additionally, the curves start to exhibit a serrated flow for HPT-processed samples annealed at $T \geq 523$ K. This flow behaviour was documented earlier for different Al-Mg-Sc alloys having UFG structures [20,38,40] and suggests the occurrence of dynamic strain ageing (DSA). It should be noted that the uniform elongation continues at very low values and strain hardening becomes more prominent when the HPT-processed metal undergoes annealing at $T \geq 623$ K.

A comparison of Figs 1 (a) and (b) shows that the material processed by HPT at RT exhibits higher flow stresses immediately after processing and after annealing up to $T = 523$ K than the same alloy processed at 450 K and annealed at similar conditions. This trend is more readily visible in Fig. 2 that depicts the yield stress (σ_y), tensile strength (σ_u) and elongation to failure ($\Delta L/L_0$, where ΔL and L_0 are the increase in length and the initial length, respectively) as a function of annealing temperature for the curves presented in Fig. 1. The datum points in Figs 1 (a) and (b) follow the same tendency of the plots of microhardness vs annealing temperature displayed in earlier reports [35,50]. In practice, annealing up to $T = 423$ K leads to a slight reduction in the yield strength of the HPT-processed samples. Conversely, the decrease in the σ_y values with increasing temperatures becomes more significant when the annealing is performed at $473 \text{ K} \leq T \leq 623$ K. For $T \geq 623$ K, σ_y continues to decrease with increasing annealing temperatures but at a much lower rate.

The variation of the tensile strength as a function of annealing temperature is very similar to the trend already described for the yield stress. Nevertheless, annealing at 423 K promoted a more sizable reduction in the σ_u values when compared with the material

processed by 10 HPT revolutions at RT. It follows from Fig. 2 (c) that the elongations achieved in the HPT-processed alloy increase with increasing annealing temperatures and the plots exhibit a general sigmoidal shape. It is important to note that annealing at 523-573 K leads to very sharp increases in the $\Delta L/L_0$ values and this is especially evident for the alloy processed by HPT at 450 K and further annealed at 523 K.

3.2 Microstructures after HPT

Table 1 summarizes the values calculated using the XRD profiles shown Fig. 1A of the Supplementary Material in Maud software for the crystallite size, the microstrain and the density of dislocations after processing through 10 HPT turns at 300 and 450 K, respectively. It is apparent that processing at 450 K led to a slightly larger crystallite size (~190 nm) than HPT at RT (~160 nm). However, both the microstrain and the dislocation density are significantly lower in the material processed at the higher temperature. This is attributed to the faster recovery kinetics at a homologous temperature of ~0.5 when compared with processing at RT ($T_H \approx 0.3$).

Fig. 3 shows typical orientation maps obtained at positions located at ~3 mm from the centre of the Al-3Mg-0.2Sc discs subjected to 10 HPT revolutions at either 300 or 450 K. The low-angle grain boundaries (LAGBs) with misorientation angles between 2 and 15^o are coloured in gray whereas the high-angle grain boundaries (HAGBs) correspond to black lines. The results in Fig. 3 demonstrate that the grain structures in the Al-Mg-Sc alloy processed at different temperatures exhibit similar sizes but are slightly elongated in the material processed by HPT at RT. Additionally, there appears to exist a larger area of grains whose {110} planes are parallel to the thickness direction in the alloy processed at RT. By contrast, HPT at 450 K gives a microtexture with a more prominent participation of grains having {111} planes parallel to the disc thickness.

The data collected in the EBSD scans is presented in Fig. 4 as histograms showing (a) the variation in the area fraction of grain diameters measured using the circle

equivalent method and (b) the fraction of correlated boundaries as a function of the misorientation angle. It is readily seen that the distributions of grain diameters show a close resemblance for both HPT temperatures although it is somewhat broader after HPT at *RT*. The area-weighted grain size (*d*) calculated for both HPT conditions is ~0.32 μm.

Inspection of in Fig. 4 (b) reveals that the misorientation distributions marginally deviate from the theoretical Mackenzie distribution (black contours) for a random array of grain structures [51]. This is due to the presence of a small number of LAGBs which corresponds to ~20% of the correlated boundaries used to construct the histogram for the material processed by HPT at 300 K.

Fig. 5 gives representative bright field (BF) TEM micrographs and their corresponding SAED patterns showing the dislocation and grain structures in the alloy processed by HPT at RT and 450 K. It is evident that the grain structures in the material processed at 300 K exhibit higher aspect ratios than after HPT at 450 K. This suggests the occurrence of a mechanically-driven process of boundary migration during HPT at RT as documented for other materials processed at low T_H [33,52]. On the other hand, the alloy deformed at 450 K exhibits a uniform array of equiaxed grains which usually follows from thermally-assisted boundary migration [52].

The SAED patterns in both microstructures exhibit annular shapes which are consistent with the EBSD results and indicate that the grains are separated mainly by HAGBs. It is important to highlight that Al_3Sc particles were not detected in the microstructures of the solution-treated alloy after 10 HPT revolutions at either 300 or 450 K. Furthermore, some of the grains display a few internal dislocations and they are not arranged in the form of cells at this stage of processing.

The linear intercept method was used to estimate the average grain boundary spacing ($\bar{L}$) using several TEM micrographs and the orientation maps shown in Fig. 3. The calculations based on the TEM images gave grain boundary spacings of ~140 and

150 nm for the alloy processed by HPT at *RT* and 450 K, respectively, whereas $\bar{L}$ was estimated as ~170 nm from the EBSD maps for both HPT temperatures. These results are consistent with earlier investigations in which a grain size of ~150 nm was measured for Al-3Mg [25,29] and Al-3Mg-0.2Sc [25] alloys after 5-10 HPT turns at RT.

3.3 Microstructures after annealing

Fig. 6 presents typical orientation maps for the Al-3Mg-0.2Sc alloy processed through 10 HPT revolutions at 300 K and subsequently annealed for 1 h at various temperatures. Inspection of Figs 6 (a) and (b) reveals that after heating at 523 and 573 K the microstructures of the alloy have very few LAGBs and are mainly constituted by equiaxed arrays of submicrometre grains with mean diameters of ~0.56 and 0.67 μm for these two temperatures, respectively.

An increase in the annealing temperature to the range of 623-673 K leads to the development of a bimodal distribution of grain sizes as is evident in Figs 6 (c) and (d) and this is shown in more detail in the form of histograms in Fig. 2A of the Supplementary Material. There remain existing UFG structures but nevertheless they correspond to an area fraction of < 30 % after heating at 673 K. Conversely, the remaining microstructure exhibits grains with sizes of the order of tens of micrometres and they appear preferably oriented with the {110} and {100} planes parallel to the disc thickness. Additional increases in the annealing temperature to the interval of 723-773 K promotes the formation of a uniform distribution of grains having a similar microtexture when compared with the abnormally larger grains developed during annealing at 623-673 K.

The microstructural evolution after annealing of the alloy processed by HPT at 450 K is presented in the orientation maps in Fig. 7. As with the material processed by HPT at RT, annealing at temperatures ranging from 523 to 573 K promotes the formation of equiaxed grain structures in the material processed originally at 450 K. However, these

grains achieve smaller sizes after annealing as follows from plots of the mean grain diameter as a function of temperature in Fig. 8.

Similarly, annealing at 623-673 K promotes the onset of a duplex distribution of grain sizes. Nevertheless, the grains with sizes in the submicrometre range constitute a much larger fraction of the microstructure and exceeding an area fraction of 70% after annealing at 673 K. The group of larger grains also attains markedly smaller sizes. It should be further noted that the grain structures at this temperature range display grains with {110} and {111} planes lying parallel to the thickness direction.

A homogenous array of grain structures with average diameters up to ~5 μm developed in the alloy processed by HPT at 450 K after heat treatments at 723-773 K. By contrast with the alloy processed by HPT at ~300 K, a minor population of grains displays {110} planes oriented towards the thickness direction but the microtexture is mostly formed by {100} and {111} planes parallel to this direction. It is therefore evident from Fig. 8 that HPT at 450 K leads to a slower kinetics of grain growth and this is especially noted for annealing temperatures between 623 and 673 K.

Histograms showing the distributions of correlated boundaries as a function of misorientation angles after annealing are displayed in Fig. 3A of the Supplementary Material. They demonstrate there are no sizable differences between the distributions obtained at comparable temperatures, except at T = 623 and 673 K where the alloy originally processed at RT exhibits a significantly larger fraction of LAGBs.

To provide information concerning the nature, size, and distribution of second phase particles in the Al-3Mg-0.2Sc alloy after annealing for 1 h at 673 K, TEM and High-Resolution TEM (HRTEM) micrographs are shown in Figs 9 and 10 for the samples processed by HPT at either 300 or 450 K, respectively. The TEM micrographs reveal the occurrence of extensive precipitation of Al_3Sc particles during heating at 673 K for HPT discs initially processed at either temperature. Examination of the dispersoid morphology

suggests that most of these phases exhibit a coffee-bean-like appearance, suggesting a coherency with the Al matrix even after 1 h of annealing. In the lower region of Fig 9 (c), there is evidence for the presence of nano-sized dispersoids in the metal processed by HPT at RT. These dispersoids exhibit radii of less than ~5 nm and are closely spaced and partially coherent with the Al matrix, as suggested from their characteristic coffee-bean-like contrast and confirmed in the HRTEM images in Figs 9 (e) and (f).

Nevertheless, Al_3Sc particles with diameters exceeding ~25 nm become incoherent with the Al matrix, as shown clearly in the HRTEM image in Fig. 9 (d). It should be noted, however, that there are a few Al_3Sc precipitates having notably larger sizes in the range of hundreds of nanometres. These particles probably correspond to Al_3Sc precipitates that were not fully dissolved during the initial solution treatment and remain stable ever after HPT processing followed by annealing at 673 K. Furthermore, the interspacing distance between precipitates is significantly larger near the coarse particles, which is apparent in the micrographs in Figs 9 and 10. It should be noted that the bi-dimensional TEM images are direct projections of 3D volumes. Consequently, Al_3Sc precipitates may misleadingly overlap and thereby give a deceptive impression of larger phases, as follows from Figs 9 (e) and (f) for the alloy initially processed by HPT at RT.

It is also evident in Fig. 10 that a few of the grain boundaries are pinned by Al_3Sc precipitates and these boundaries exhibit clear bulges suggesting the occurrence of strain-induced grain boundary migration delayed by the Zener pinning effect. Fig. 11 displays histograms showing the size distributions of the Al_3Sc nanoparticles for the Al-Mg-Sc discs subjected to 10 HPT revolutions at either RT or 450 K followed by annealing at 673 K. These plots were generated by measuring the radii of precipitates (r) using the circle equivalent method in Image J software with representative TEM micrographs having high

magnifications as in Figs 9 (c) and 10 (e). In these calculations, totals of 153 and 192 particles were recorded for discs initially processed by HPT at RT or 450 K, respectively.

The histograms presented in Fig. 11 demonstrate that the HPT discs exhibit similar size distributions after annealing, even though it is apparent that Al_3Sc phases with lower radii are detected for the alloy subjected to HPT at 450 K. After annealing at 673 K, the mean radius of the nanoparticles was estimated as ~3.2 and 3.3 nm for the Al-Mg-Sc alloy processed by 10 HPT turns at RT or 450 K, respectively. These values show reasonable agreement with earlier experiments undertaken on an Al-0.25Sc alloy [53] where an average precipitate radius of ~3.5 nm was recorded after heating under similar conditions.

4. Discussion

4.1 Flow properties after HPT at different temperatures and further annealing

The results of this research reveal that the application of 10 HPT revolutions at 300 and 450 K to the solution-treated Al-3Mg-0.2Sc alloy successfully promotes the development of a uniform array of submicrometre grains with average diameters of ~320 nm. It should be noted, however, that an increased contribution of dynamic recovery during 450 K HPT at $T_H \approx 0.5$ promotes both the formation of more equiaxed grain structures and the partial annihilation of dislocations and this leads to much lower ρ values by comparison with the same alloy after HPT at RT (see Table 1). These microstructural features allow the achievement of values of $\sigma_y \approx 550$ and 600 MPa immediately after processing at 450 K and RT, respectively, as shown in Fig. 1.

After annealing for 1 h at 423 K, the tensile strength of the alloy subjected to HPT at RT decreases from ~680 to 580 MPa whereas there is only a minor reduction in σ_u for the alloy processed at 450 K. These differences are associated with the occurrence of static recovery which has a more prominent effect in the material originally processed at RT as it displays a higher density of dislocations prior to annealing. The results in Figs 6,

7 and 8 reveal that grain coarsening becomes evident after annealing at $T \geq 523$ K. This is consistent with the drops in the values of σ_y and σ_u shown in Fig. 2.

Nevertheless, it is important to emphasize that the grains structures in the HPT-processed material continue to exhibit average sizes < 1 μm after heating at temperatures of 523-573 K. Also, there is evidence of further grain growth, the formation of a duplex structure and precipitation of Al_3Sc particles at temperatures ranging from 623 to 673 K. It is well-known that the Hall-Petch relationship [54–56] may be used to predict the effect of grain boundary strengthening at RT in Al alloys as shown in the following equation:

$$\sigma_y = \sigma_0 + kd^{-0.5} \quad (2)$$

where σ_0 and k are alloy constants. To better understand the microstructural changes associated with material strength during annealing, Fig. 12 shows plots of σ_y *vs* $d^{-0.5}$ and σ_u *vs* $\Delta L/L_0$ for the alloy processed by HPT at either 300 or 450 K and further annealed for 1 h at temperatures within the interval of 423 to 773 K.

It is readily apparent in Fig 12 (a) that the values of σ_y and $d^{-0.5}$ do not lie in a single line as expected if the Hall-Petch equation was uniquely sufficient to predict the flow behaviour. On the contrary, the datum points can be divided into three regions based on the observed trends. For the region with $d^{-0.5}$ > 1400 $m^{-0.5}$, there is an increasing strength with decreasing grain size and the data belonging to this interval correspond to material in the HPT-processed state and after annealing at 523 and 573 K. The HPT-processed alloy reaches σ_y values > 500 MPa and there is a consistent reduction in σ_y after heating at 523 and 573 K.

Regardless of the HPT processing temperature, the Al-Mg-Sc alloy annealed at 523-573 K exhibited grain coarsening and probably a decrease in the density of dislocations by comparison with the HPT-processed states. This is consistent with the increases in the fractions of HAGBs in the orientation maps as shown in Fig. 3A in the

Supplementary Material and the higher elongations achieved during tensile testing as highlighted with a blue oval in Fig. 12 (b). There is also evidence that deformation is controlled by dynamic strain ageing due to the onset of type B Portevin-Le Chatelier (PLC) serrations in the stress-strain curves in Fig. 1 which contribute to the increased ductility during tensile testing, where this matches results for a UFG Al-6Mg-0.2Sc alloy deformed under comparable conditions [38,57].

It should be noted that the time exposure during annealing at 523 K (1 h) was probably not sufficient to promote the precipitation of Al_3Sc particles in the supersaturated alloy but the formation of coherent dispersoids in supersaturated Al-Sc alloys has been documented after 8 passes of ECAP at T = 573 K [58] and after ageing at 573 K for shorter times [8]. Accordingly, the most prominent strengthening mechanisms in the Al-Mg-Sc alloy heat treated up to T = 523 K are probably grain boundary, dislocation and solid solution strengthening whereas the contribution from the precipitation becomes relevant only for $T \geq 573$ K.

It is surprisingly revealed in Fig. 12 (a) that, although an increase in the annealing temperature from 573 to 623 K promotes a marked reduction in the grain sizes, in practice the HPT discs processed at RT or 450 K exhibit very similar yield strengths. This follows from the analogous ageing kinetics for the Al-Mg-Sc alloy at 573 and 623 K which generate homogeneous arrays of coherent particles with radii below 2 nm after heating at comparable conditions [8,9,59]. It has been shown that Al-Sc alloys achieve a peak ageing condition for Al_3Sc particles having r values ranging from ~1 to 2 nm and this led to an increment in σ_y up to ~180-210 MPa by comparison with the supersaturated alloy [59]. For this reason, the yield strength in the Al-3Mg-0.3Sc alloy after annealing at 573-673 K is insensitive to the grain size since the mean free path for dislocation motion is determined instead by the particle interspacing. Furthermore, DSA together with shearing of coherent dispersoids are almost certainly the prevalent deformation mechanisms [59].

Finally, it is interesting to note that there is an abrupt decrease in the σ_y values when annealing is conducted at $T \geq 673$ K. This change in the flow behaviour is attributed to the onset of discontinuous precipitation of the Al_3Sc dispersoids as also documented for other Al-Sc alloys at $T \geq 643$ K [8]. In this temperature range, the precipitates preferably nucleate at dislocations and grain boundaries and they become progressively larger with increasing temperature [60]. Also, the Al_3Sc particles eventually lose their coherency with the Al matrix as is apparent from the TEM observations.

This phenomenon is consistent with the mechanical behaviour and microstructural features of the Al-3Mg-0.2Sc alloy annealed at 673 K as the occurrence of heterogenous precipitation renders areas having depleted fractions of dispersoids. These regions correspond to abnormally grown grains whose interiors exhibit larger free paths for dislocation motion and are thus softer than the remaining areas encompassing UFGs and more closely spaced particles. Consequently, plastic straining is probably first triggered within the areas having larger grains and fewer Al_3Sc particles and this is consistent with the decreasing yield strength with increasing annealing temperature.

It should be noted that, although σ_y appears to decrease with increasing grain sizes for annealing at $T \geq 673$ K, it is unlikely that grain boundary strengthening becomes again predominant because the mean free path is consistently determined by the precipitate interspacing. There may also occur a gradual change in the deformation mechanism from precipitate shearing to Orowan looping due to the increasing presence of nonshearable particles as reported for other Al-Sc alloys [59,61]. This is consistent with the occurrence of considerable work-hardening in the HPT-processed alloy deformed at RT after annealing at $T \geq 673$ K. It also explains the increased elongations attained during tensile testing [38,62]. Furthermore, DSA remains prevalent during deformation at RT as follows from the presence of oscillations in the stress-strain curves. Nevertheless, the PLC

serrations are now from types B + C which are consistent with the increase in grain size with increasing temperature [38,39,57].

4.2 Microstructural Stability after HPT at different temperatures

This research demonstrates that the microstructural stability of Al-Mg alloys with Sc additions is markedly improved by conducting HPT at 450 K as the Al-3Mg-0.2Sc alloy displays a more homogenous array of grain structures with lower sizes after annealing for the same duration and temperature. The reasons underlying this conclusion can be evaluated through a calculation of the restraining pressure due to the Zenner pinning effect (P_z) and the driving pressures for boundary migration associated with the release of the internal energy due to stored dislocations (P_d) and the grain boundary energy (P_g) as expressed in the following equations [63]:

$$P_z = k\frac{f\gamma}{r} \tag{3}$$

where k is a shape factor equal to 1.5 for spherical precipitates, γ is the energy associated with HAGBs and f and r are the volume fraction and the mean precipitate radius,

$$P_d = 0.5\, G\, \mathbf{b}\, \rho^{1/2} \tag{4}$$

where G is the shear modulus and

$$P_g = \frac{3\gamma}{d} \tag{5}$$

Table 2 displays the values estimated for f considering equilibrium conditions for the Al-Sc phase diagram [7] together with the precipitate radii obtained in this research and in other studies for solubilised Al-Sc alloys having similar compositions [9,53] after heat treatment at temperatures from 573 to 773 K. The values calculated for P_z using eq. (3) are also tabulated. The results reveal that the high fraction of Al_3Sc precipitates with radii below 2 nm leads to pinning pressures > 1.0 MPa as predicted for the Al-3Mg-0.2Sc alloy after annealing for 1 h at 573-623 K. Conversely, the P_z values are drastically

reduced at higher temperatures and are lower than 0.1 MPa after heating at 773 K. It should be further noted that the r values measured in this research show excellent agreement with the values reported for an Al-0.25Sc alloy annealed for ~1 h [53].

The driving pressures for the HPT-processed Al-3Mg-0.2Sc alloy were calculated using eq. (4) and (5) with G = 25.42 GPa, $\mathbf{b} = 2.86 \times 10^{-10}$ m [64] and $\gamma = 0.324$ Jm^{-2} [65]. The estimated values of P_d and P_g are shown in Table 3 together with the sum of the driving and restraining pressures ($\Sigma P = P_g + P_d - P_z$) for migration of HAGBs. It follows from Table 3 that the pressure due to stored dislocations appears to play a minor role by comparison with P_g regarding the potential for recrystallisation. The interfacial energy due to the presence of grain diameters of ~320 nm is three orders of magnitude higher than P_d, considering the dislocation densities predicted using the XRD profiles. Nevertheless, $\Sigma P > 0$ for all annealing temperatures in Table 3 and this suggests that grain coarsening may occur if the grain boundary mobilities are sufficiently high [63,66].

A thorough comparison of the ΣP values in Table 3 reveals, surprisingly, that there is no significant difference in the net pressure for boundary migration in the material processed by HPT at either 300 or 450 K for heat treatments conducted at similar conditions. Therefore, in order to fully understand the reasons for the superior microstructural stability after HPT at 450 K it is first necessary to consider that the velocity of the moving boundary (v) is expressed as follows [63,66]:

$$v = M \, \Sigma P \tag{6}$$

where M is the grain boundary mobility.

The grain boundary mobility increases with increasing temperature and may decrease due to segregation of solute atoms at grain boundaries [33,63,66]. Furthermore, the M values depend upon the boundary orientation to their neighbouring grains such that, in general, more closely-packed grain contours display lower mobilities [63]. Also, some

orientation relationships may exhibit extremely high mobilities as reported in Al alloys for <111> tilt boundaries with misorientation angles of ~40^{o} [66,67].

However, in this investigation, there is no evidence for the occurrence of solute segregation in the Al-3Mg-0.2Sc alloy after 10 HPT revolutions for both processing temperatures. Additionally, the orientation maps after annealing are not conclusive in revealing a particular orientation relationship having consistently faster growth rates. Thus, the enhanced thermal stability in the Al-Mg-Sc alloy processed by HPT at 450 K may be associated with a more homogenous microstructure than after processing by HPT at RT.

The Al-Mg-Sc alloy processed at 300 K exhibits a notably higher density of dislocations which are heterogeneously distributed throughout the HPT disc. It also displays grains with higher aspect ratios and a broader size distribution. Therefore, these local gradients may provide conditions for either triggering the discontinuous precipitation of Al_3Sc particles or they may promote boundary motion at faster rates during heating if this latter phenomenon precedes the precipitation of large numbers of nanosized Al_3Sc particles. Nevertheless, further studies are now needed to more fully elucidate the reasons for the superior thermal stability encountered after HPT at 450 K.

The susceptibility for abnormal grain growth in alloys with second phases can be analysed by calculating a boundary stability factor (ψ) defined as follows [68]:

$$\psi = \frac{k\ f\ d}{2r} \tag{7}$$

The application of Eq. (7) assumes a broadening in the distribution of grain sizes which can be expressed as the ratio between the diameter of a single grain and the mean grain size [68]. According to this model, abnormal coarsening occurs when $0.25 < \psi < 1$ and this may arise concurrently with normal grain growth for $0.1 < \psi < 0.25$. For $\psi < 0.1$,

the distribution of grain sizes may show some dispersion and grain growth should not be detected for $\psi > 1$. The various ψ values estimated in this study are given in Table 3.

The boundary stability factor is estimated as ~1.20 MPa in the Al-Mg-Sc alloy after heat treatment at 573 K. At first sight, this apparently contradicts the model used to derive Eq. 7 but nevertheless the calculations of ψ considered the mean precipitate radii achieved at the end of annealing. It is possible, therefore, that boundary motion started before precipitation and the HAGBs were effectively hindered only after the formation of a critical number of nanosized particles. The ψ values for the Al-3Mg-0.2Sc alloy range from 0.64 to 0.35 after annealing at 623 and 673 K and this is consistent with the current results as abnormal grain coarsening was detected at these temperatures. After annealing at $T \geq 723$ K, the distribution of grain sizes in the Al-Mg-Sc alloy is reasonably uniform and this also agrees with the model as follows from the ψ values shown in Table 3.

For convenience, Fig. 13 shows schematically the most relevant microstructural changes occurring during heating for the Al-3Mg-0.2Sc alloy processed through 10 HPT turns at different temperatures. These illustrations demonstrate that after HPT at 300 or 450 K there is no precipitation of Al_3Sc dispersoids and the microstructures are composed of a homogenous array of ultrafine grains having similar overall sizes. Nevertheless, the grains are less elongated after processing at a high homologous temperature and there are then fewer free dislocations. Annealing at T_H up to ~0.60 leads to a minor increase in the overall size of the grains and a reduction in the fraction of LAGBs. These combined factors produce a decrease in the yield and tensile strengths and permit the achievement of higher elongations during tensile testing at RT.

An increase in the homologous temperature to ~0.65-0.75 produces abnormal grain coarsening in the Al microstructure and this occurs concurrently with the heterogeneous nucleation of Al_3Sc dispersoids [69]. Conversely, the Al-3Mg-0.2Sc alloy displays a uniform array of grains having larger sizes after heating at $T_H > 0.75$. This

follows from the higher boundary mobilities at these temperatures which permit the fast migration of grain boundaries prior to the precipitation of a large number of nano-sized particles [60]. The ageing kinetics are also accelerated at high homologous temperatures and this leads to particle coarsening and the achievement of larger equilibrium grain sizes.

5. Summary and conclusions

1- A solution-treated Al-3Mg-0.2Sc alloy was subjected to 10 HPT revolutions at RT ≈ 300 K or at 450 K to produce a uniform array of grains with an average diameter of ~320 nm. Tensile testing together with XRD, EBSD and TEM analyses were conducted after processing and after subsequent annealing for 1 h at temperatures (T) up to 773 K.

2- After HPT at RT, the alloy achieved yield and tensile strengths of ~590 and 680 MPa, respectively. These values are significantly higher than after HPT at 450 K even though the microstructures of the Al-Mg-Sc alloy displayed nearly the same grain sizes. This is attributed to the higher density of stored dislocations after processing at ~300 K.

3- There was evidence for the occurrence of dynamic strain ageing (DSA) during deformation at RT for the HPT-processed Al-Mg-Sc alloy annealed at $T \geq 523$ K. Type B Portevin-Le Chatelier serrations were recorded in the flow curves after heat treatment at 523-573 K and there was a transition from type B to type C oscillations for $T \geq 623$ K.

4- Grain boundary, dislocation and solid solution strengthening are the main mechanisms operating during tensile testing at RT for the Al-3Mg-0.2Sc alloy after HPT processing and after annealing up to $T \approx 523$ K. For $T \geq 573$ K, the contribution from precipitation becomes relevant as the mean free path for dislocation motion is primarily determined by the interspacing between Al_3Sc particles.

5- HPT at 450 K produces grain structures with greater thermal stability in the Al-3Mg-0.2Sc alloy than processing at 300 K. This may originate from the higher density of heterogeneously distributed dislocations along the microstructure formed during HPT at

RT as the local gradients may either trigger grain boundary migration at faster rates or provide conditions for the discontinuous precipitation of Al_3Sc particles during heating.

6- The grain structures of the HPT-processed material underwent abnormal growth during annealing at $623 < T < 673$ K and this was not observed at other temperatures. This is consistent with the values calculated for the boundary stability factor (ψ) using a theoretical model derived for alloys having second-phase particles.

Data availability

The raw/processed data required to reproduce these findings can be shared upon request.

Acknowledgements

This research was supported by the European Research Council under ERC Grant Agreement No. 267464-SPDMETALS (TGL and YH), FAPEMIG under Grant APQ-01342–21 (PHRP) and CNPq under Grant No. 443736/2018–9 (PHRP).

References

[1] W.S. Miller, L. Zhuang, J. Bottema, A.J. Wittebrood, P. De Smet, A. Haszler, A. Vieregge, Recent development in aluminium alloys for the automotive industry, Materials Science and Engineering: A. 280 (2000) 37–49. https://doi.org/10.1016/S0921-5093(99)00653-X.

[2] C. Gao, S. Wolff, S. Wang, Eco-friendly additive manufacturing of metals: Energy efficiency and life cycle analysis, J Manuf Syst. 60 (2021) 459–472. https://doi.org/10.1016/J.JMSY.2021.06.011.

[3] M. Kleiner, M. Geiger, A. Klaus, Manufacturing of Lightweight Components by Metal Forming, CIRP Ann Manuf Technol. 52 (2003) 521–542. https://doi.org/10.1016/S0007-8506(07)60202-9.

[4] O.C. Haase, P.R. Cetlin, R.B. Figueiredo, T.G. Langdon, P.H.R. Pereira, Tailoring a high-strength Al–4Cu alloy through processing of powders by up to 100 turns of high-pressure torsion, Materials Science and Engineering: A. 882 (2023) 145454. https://doi.org/10.1016/J.MSEA.2023.145454.

[5] Y.A. Filatov, V.I. Yelagin, V. V Zakharov, New Al–Mg–Sc alloys, Materials Science and Engineering: A. 280 (2000) 97–101. https://doi.org/http://dx.doi.org/10.1016/S0921-5093(99)00673-5.

[6] X. Yu, D. Yin, Z. Yu, Effects of Cerium and Zirconium Microalloying Addition on the Microstructures and Tensile Properties of Novel Al-Cu-Li Alloys, Rare Metal Materials and Engineering. 45 (2016) 1917–1923. https://doi.org/10.1016/S1875-5372(16)30147-3.

[7] J. Røyset, N. Ryum, Scandium in aluminium alloys, International Materials Reviews. 50 (2005) 19–44. https://doi.org/10.1179/174328005X14311.

[8] J. Røyset, N. Ryum, Kinetics and mechanisms of precipitation in an Al-0.2wt.% Sc alloy, Materials Science and Engineering A. 396 (2005) 409–422. https://doi.org/10.1016/j.msea.2005.02.015.

[9] E.A. Marquis, D.N. Seidman, Nanoscale structural evolution of Al3Sc precipitates in Al(Sc) alloys, Acta Mater. 49 (2001) 1909–1919. https://doi.org/10.1016/S1359-6454(01)00116-1.

[10] E.A. Marquis, D.N. Seidman, M. Asta, C. Woodward, Composition evolution of nanoscale Al3Sc precipitates in an Al-Mg-Sc alloy: Experiments and computations, Acta Mater. 54 (2006) 119–130. https://doi.org/10.1016/j.actamat.2005.08.035.

[11] J. Wang, M. Furukawa, Z. Horita, M. Nemoto, R.Z. Valiev, T.G. Langdon, Enhanced grain growth in an Al-Mg alloy with ultrafine grain size, Materials Science and Engineering: A. 216 (1996) 41–46. https://doi.org/10.1016/0921-5093(96)10390-7.

[12] J. Wang, Y. Iwahashi, Z. Horita, M. Furukawa, M. Nemoto, R.Z. Valiev, T.G. Langdon, An investigation of microstructural stability in an Al-Mg alloy with submicrometer grain size, Acta Mater. 44 (1996) 2973–2982. https://doi.org/10.1016/1359-6454(95)00395-9.

[13] S. Lee, A. Utsunomiya, H. Akamatsu, K. Neishi, M. Furukawa, Z. Horita, T.G. Langdon, Influence of scandium and zirconium on grain stability and superplastic ductilities in ultrafine-grained Al-Mg alloys, Acta Mater. 50 (2002) 553–564. https://doi.org/10.1016/S1359-6454(01)00368-8.

[14] T.G. Langdon, Twenty-five years of ultrafine-grained materials: Achieving exceptional properties through grain refinement, Acta Mater. 61 (2013) 7035–7059. https://doi.org/10.1016/j.actamat.2013.08.018.

[15] K. Edalati, A. Bachmaier, V.A. Beloshenko, Y. Beygelzimer, V.D. Blank, W.J. Botta, K. Bryła, J. Čížek, S. Divinski, N.A. Enikeev, Y. Estrin, G. Faraji, R.B. Figueiredo, M. Fuji, T. Furuta, T. Grosdidier, J. Gubicza, A. Hohenwarter, Z. Horita, J. Huot, Y. Ikoma, M. Janeček, M. Kawasaki, P. Král, S. Kuramoto, T.G. Langdon, D.R. Leiva, V.I. Levitas, A. Mazilkin, M. Mito, H. Miyamoto, T. Nishizaki, R. Pippan, V. V. Popov, E.N. Popova, G. Purcek, O. Renk, Á. Révész, X. Sauvage, V. Sklenicka, W. Skrotzki, B.B. Straumal, S. Suwas, L.S. Toth, N. Tsuji, R.Z. Valiev, G. Wilde, M.J. Zehetbauer, X. Zhu, Nanomaterials by severe plastic deformation: review of historical developments and recent advances, Mater Res Lett. 10 (2022) 163–256. https://doi.org/10.1080/21663831.2022.2029779.

[16] R.Z. Valiev, T.G. Langdon, Principles of equal-channel angular pressing as a processing tool for grain refinement, Prog Mater Sci. 51 (2006) 881–981. https://doi.org/10.1016/J.PMATSCI.2006.02.003.

[17] A.P. Zhilyaev, T.G. Langdon, Using high-pressure torsion for metal processing: Fundamentals and applications, Prog Mater Sci. 53 (2008) 893–979. https://doi.org/10.1016/j.pmatsci.2008.03.002.

[18] K. Edalati, Z. Horita, A review on high-pressure torsion (HPT) from 1935 to 1988, Materials Science and Engineering A. 652 (2016) 325–352. https://doi.org/10.1016/j.msea.2015.11.074.

[19] P.H.R. Pereira, Y. Huang, M. Kawasaki, T.G. Langdon, An examination of the superplastic characteristics of Al–Mg–Sc alloys after processing, J Mater Res. 32 (2017) 4541–4553. https://doi.org/10.1557/jmr.2017.286.

[20] P.H.R. Pereira, Y.C. Wang, Y. Huang, T.G. Langdon, Influence of grain size on the flow properties of an Al-Mg-Sc alloy over seven orders of magnitude of strain rate, Materials Science and Engineering A. 685 (2017) 367–376. https://doi.org/10.1016/j.msea.2017.01.020.

[21] T.G. Langdon, A unified approach to grain boundary sliding in creep and superplasticity, Acta Metallurgica et Materialia. 42 (1994) 2437–2443. https://doi.org/10.1016/0956-7151(94)90322-0.

[22] T.G. Langdon, Seventy-five years of superplasticity: Historic developments and new opportunities, J Mater Sci. 44 (2009) 5998–6010. https://doi.org/10.1007/s10853-009-3780-5.

[23] T.G. Langdon, An evaluation of the strain contributed by grain boundary sliding in superplasticity, Materials Science and Engineering, A. 174 (1994) 225–230. https://doi.org/https://doi.org/10.1016/0921-5093(94)91092-8.

[24] S. Komura, Z. Horita, M. Furukawa, M. Nemoto, T.G. Langdon, Influence of scandium on superplastic ductilities in an Al-Mg-Sc alloy, J Mater Res. 15 (2000) 2571–2576. https://doi.org/10.1557/JMR.2000.0367.

[25] G. Sakai, Z. Horita, T.G. Langdon, Grain refinement and superplasticity in an aluminum alloy processed by high-pressure torsion, Materials Science and Engineering: A. 393 (2005) 344–351. https://doi.org/10.1016/j.msea.2004.11.007.

[26] P.H.R. Pereira, Y. Huang, T.G. Langdon, Thermal stability and superplastic behaviour of an Al-Mg-Sc alloy processed by ECAP and HPT at different temperatures, IOP Conf Ser Mater Sci Eng. 194 (2017) 012013. https://doi.org/10.1088/1757-899X/194/1/012013.

[27] P.H.R. Pereira, Y. Huang, T.G. Langdon, Examining the mechanical properties and superplastic behaviour in an Al-Mg-Sc alloy after processing by HPT, Letters on Materials. 5 (2015) 294–300.

[28] S. Komura, Z. Horita, M. Furukawa, M. Nemoto, T.G. Langdon, An evaluation of the flow behavior during high strain rate superplasticity in an Al-Mg-Sc alloy, Metall Mater Trans A Phys Metall Mater Sci. 32 (2001) 707–716. https://doi.org/10.1007/s11661-001-1006-9.

[29] D.C. Machado, P.C. Alves Flausino, Y. Huang, P.R. Cetlin, T.G. Langdon, P.H.R. Pereira, Influence of processing temperature on microhardness evolution, microstructure and superplastic behaviour in an Al–Mg alloy processed by high-pressure torsion, Journal of Materials Research and Technology. 24 (2023) 2850–2867. https://doi.org/10.1016/J.JMRT.2023.03.167.

[30] X. Sauvage, A. Duchaussoy, G. Zaher, Strain Induced Segregations in Severely Deformed Materials, Mater Trans. 60 (2019) 1151–1158. https://doi.org/10.2320/matertrans.MF201919.

[31] F. Abdeljawad, S.M. Foiles, Stabilization of nanocrystalline alloys via grain boundary segregation: A diffuse interface model, Acta Mater. 101 (2015) 159–171. https://doi.org/10.1016/j.actamat.2015.07.058.

[32] A. Devaraj, W. Wang, R. Vemuri, L. Kovarik, X. Jiang, M. Bowden, J.R. Trelewicz, S. Mathaudhu, A. Rohatgi, Grain boundary segregation and intermetallic precipitation in coarsening resistant nanocrystalline aluminum alloys, Acta Mater. 165 (2019) 698–708. https://doi.org/10.1016/j.actamat.2018.09.038.

[33] I.C. dos Santos, E.M. Mazzer, R.B. Figueiredo, T.G. Langdon, P.H.R. Pereira, Evidence for two-stage hardening in an Al-Zn-Mg-Cu alloy processed by high-pressure torsion, J Alloys Compd. 941 (2023) 10.1016. https://doi.org/10.1016/j.jallcom.2023.168839.

[34] G. Sha, L. Yao, X. Liao, S.P. Ringer, Z.C. Duan, T.G. Langdon, Segregation of solute elements at grain boundaries in an ultrafine grained Al-Zn-Mg-Cu alloy, Ultramicroscopy. 111 (2011) 500–505. https://doi.org/10.1016/j.ultramic.2010.11.013.

[35] P.H.R. Pereira, Y. Huang, T.G. Langdon, Examining the microhardness evolution and thermal stability of an Al–Mg–Sc alloy processed by high-pressure torsion at

a high temperature, Journal of Materials Research and Technology. 6 (2017) 348–354. https://doi.org/10.1016/j.jmrt.2017.05.008.

[36] P. Ghosh, O. Renk, R. Pippan, Microtexture analysis of restoration mechanisms during high pressure torsion of pure nickel, Materials Science and Engineering A. 684 (2017) 101–109. https://doi.org/10.1016/j.msea.2016.12.032.

[37] S.V. Dobatkin, O.V. Rybalchenko, N.A. Enikeev, A.A. Tokar, M.M. Abramova, Formation of fully austenitic ultrafine-grained high strength state in metastable Cr-Ni-Ti stainless steel by severe plastic deformation, Mater Lett. 166 (2016) 276–279. https://doi.org/10.1016/j.matlet.2015.12.094.

[38] D. Zhemchuzhnikova, R. Kaibyshev, Mechanical Behavior of an Al-Mg-Mn-Sc Alloy with an Ultrafine Grain Structure at Cryogenic Temperatures, Adv Eng Mater. 17 (2015) 1804–1811. https://doi.org/10.1002/adem.201500138.

[39] D. Zhemchuzhnikova, M. Lebyodkin, T. Lebedkina, A. Mogucheva, D. Yuzbekova, R. Kaibyshev, Peculiar Spatiotemporal Behavior of Unstable Plastic Flow in an AlMgMnScZr Alloy with Coarse and Ultrafine Grains, Metals 2017, Vol. 7, Page 325. 7 (2017) 325. https://doi.org/10.3390/MET7090325.

[40] A. Mogucheva, D. Yuzbekova, R. Kaibyshev, T. Lebedkina, M. Lebyodkin, Effect of Grain Refinement on Jerky Flow in an Al-Mg-Sc Alloy, Metall Mater Trans A Phys Metall Mater Sci. 47 (2016) 2093–2106. https://doi.org/10.1007/s11661-016-3381-2.

[41] R.B. Figueiredo, P.R. Cetlin, T.G. Langdon, Using finite element modeling to examine the flow processes in quasi-constrained high-pressure torsion, Materials Science and Engineering A. 528 (2011) 8198–8204. https://doi.org/10.1016/j.msea.2011.07.040.

[42] P.H.R. Pereira, R.B. Figueiredo, P.R. Cetlin, T.G. Langdon, Using finite element modelling to examine the flow process and temperature evolution in HPT under different constraining conditions, IOP Conf Ser Mater Sci Eng. 63 (2014) 012041. https://doi.org/10.1088/1757-899X/63/1/012041.

[43] M. Kai, Z. Horita, T.G. Langdon, Developing grain refinement and superplasticity in a magnesium alloy processed by high-pressure torsion, Materials Science and Engineering A. 488 (2008) 117–124. https://doi.org/10.1016/j.msea.2007.12.046.

[44] P.H.R. Pereira, R.B. Figueiredo, P.R. Cetlin, T.G. Langdon, An examination of the elastic distortions of anvils in high-pressure torsion, Materials Science and Engineering A. 631 (2015) 201–208. https://doi.org/10.1016/j.msea.2015.02.052.

[45] H. Shahmir, P.H.R. Pereira, Y. Huang, T.G. Langdon, Mechanical properties and microstructural evolution of nanocrystalline titanium at elevated temperatures, Materials Science and Engineering: A. 669 (2016) 358–366. https://doi.org/10.1016/j.msea.2016.05.105.

[46] J. Gubicza, P.H.R. Pereira, G. Kapoor, Y. Huang, S.S. Vadlamani, T.G. Langdon, Annealing-Induced Hardening in Ultrafine-Grained Ni-Mo Alloys, Adv Eng Mater. 20 (2018) 1800184. https://doi.org/10.1002/adem.201800184.

[47] Y. Huang, M. Lemang, N.X. Zhang, P.H.R. Pereira, T.G. Langdon, Achieving superior grain refinement and mechanical properties in vanadium through high-pressure torsion and subsequent short-term annealing, Materials Science and Engineering A. 655 (2016) 60–69. https://doi.org/10.1016/j.msea.2015.12.086.

[48] G.K. Williamson, R.E. Smallman, Dislocation densities in some annealed and cold-worked metals from measurements on the X-ray Debye-Scherrer spectrum, Philosophical Magazine. 1 (1956) 34–46. https://doi.org/10.1080/14786435608238074.

[49] R.E. Smallman, K.H. Westmacott, Stacking faults in face-centred cubic metals and alloys, Philosophical Magazine. 2 (1957) 669–683. https://doi.org/10.1080/14786435708242709.

[50] P.H.R. Pereira, Y. Huang, T.G. Langdon, Examining the thermal stability of an Al-Mg-Sc alloy processed by high-pressure torsion, Materials Research. 20 (2017) 39–45. https://doi.org/http://dx.doi.org/10.1590/1980-5373-MR-2017-0207.

[51] J.K. Mackenzie, Second paper on statistics associated with the random disorientation of cubes, Biometrika. 45 (1958) 229–240. https://doi.org/10.2307/2333059.

[52] O. Renk, R. Pippan, Transition from thermally assisted to mechanically driven boundary migration and related apparent activation energies, Scr Mater. 154 (2018) 212–215. https://doi.org/10.1016/j.scriptamat.2018.05.052.

[53] M. Ferry, N.E. Hamilton, F.J. Humphreys, Continuous and discontinuous grain coarsening in a fine-grained particle-containing Al–Sc alloy, Acta Mater. 53 (2005) 1097–1109. https://doi.org/10.1016/J.ACTAMAT.2004.11.006.

[54] E.O. Hall, The Deformation and Ageing of Mild Steel: III Discussion of Results, Proceedings of the Physical Society. Section B. 64 (1951) 747–753. https://doi.org/10.1088/0370-1301/64/9/303.

[55] N.J. Petch, The cleavage strength of polycrystals, J. Iron Steel Inst. 174 (1953) 25–28. https://doi.org/10.1007/BF01972547.

[56] R.B. Figueiredo, M. Kawasaki, T.G. Langdon, Seventy years of Hall-Petch, ninety years of superplasticity and a generalized approach to the effect of grain size on flow stress, Prog Mater Sci. 137 (2023) 101131. https://doi.org/10.1016/J.PMATSCI.2023.101131.

[57] D.A. Zhemchuzhnikova, M.A. Lebyodkin, T.A. Lebedkina, R.O. Kaibyshev, Unusual behavior of the Portevin-Le Chatelier effect in an AlMg alloy containing precipitates, Materials Science and Engineering A. 639 (2015) 37–41. https://doi.org/10.1016/j.msea.2015.04.094.

[58] Yu. Buranova, V. Kulitskiy, M. Peterlechner, A. Mogucheva, R. Kaibyshev, S.V. Divinski, G. Wilde, Al3(Sc,Zr)-based precipitates in Al–Mg alloy: Effect of severe deformation, Acta Mater. 124 (2017) 210–224. https://doi.org/10.1016/J.ACTAMAT.2016.10.064.

[59] D.N. Seidman, E.A. Marquis, D.C. Dunand, Precipitation strengthening at ambient and elevated temperatures of heat-treatable Al(Sc) alloys, Acta Mater. 50 (2002) 4021–4035. https://doi.org/10.1016/S1359-6454(02)00201-X.

[60] M.J. Jones, F.J. Humphreys, Interaction of recrystallization and precipitation: The effect of Al3Sc on the recrystallization behaviour of deformed aluminium, Acta Mater. 51 (2003) 2149–2159. https://doi.org/10.1016/S1359-6454(03)00002-8.

[61] H. Chen, Z. Chen, G. Ji, S. Zhong, H. Wang, A. Borbély, Y. Ke, Y. Bréchet, The influence of shearable and nonshearable precipitates on the Portevin-Le Chatelier behavior in precipitation hardening AlMgScZr alloys, Int J Plast. 147 (2021) 103120. https://doi.org/10.1016/J.IJPLAS.2021.103120.

[62] J. Røyset, N. Ryum, D. Bettella, A. Tocco, Z. Jia, J.K. Solberg, O. Reiso, On the addition of precipitation- and work-hardening in an Al-Sc alloy, Materials Science and Engineering A. 483–484 (2008) 175–178. https://doi.org/10.1016/j.msea.2006.09.164.

[63] F.J. Humphreys, M. Hatherly, Recrystallization and Related Annealing Phenomena, Second edition, Pergamon Press, Oxford, 2004. https://doi.org/10.1016/B978-0-08-044164-1.X5000-2.

[64] F.A. Mohamed, T.G. Langdon, Deformation mechanism maps based on grain size, Metallurgical Transactions. 5 (1974) 2339–2345. https://doi.org/10.1007/BF02644014.

[65] L.E. Murr, Interfacial phenomena in metals and alloys, Addison-Wesley Pub. Co., Advanced Book Program, Reading (MA), 1975.

[66] Y. Huang, F.J. Humphreys, The effect of solutes on grain boundary mobility during recrystallization and grain growth in some single-phase aluminium alloys, Mater Chem Phys. 132 (2012) 166–174. https://doi.org/10.1016/J.MATCHEMPHYS.2011.11.018.

[67] Y. Huang, F.J. Humphreys, Measurements of grain boundary mobility during recrystallization of a single-phase aluminium alloy, Acta Mater. 47 (1999) 2259–2268. https://doi.org/10.1016/S1359-6454(99)00062-2.

[68] F.J. Humphreys, A unified theory of recovery, recrystallization and grain growth, based on the stability and growth of cellular microstructures - II. The effect of second-phase particles, Acta Mater. 45 (1997) 5031–5039. https://doi.org/10.1016/S1359-6454(97)00173-0.

[69] J.D. Robson, M.J. Jones, P.B. Prangnell, Extension of the N-model to predict competing homogeneous and heterogeneous precipitation in Al-Sc alloys, Acta Mater. 51 (2003) 1453–1468. https://doi.org/10.1016/S1359-6454(02)00540-2.

Figure captions:

Fig. 1. Stress *vs* strain curves obtained at RT for the Al-3Mg-0.2Sc alloy processed by HPT at (a) 300 or (b) 450 K and annealed for 1 h at temperatures from 423 to 773 K.

Fig. 2. (a) Yield stress, (b) tensile strength and (c) elongation to failure as function of annealing temperature for the Al-3Mg-0.2Sc alloy processed by HPT at (a) 300 or (b) 450 K, annealed for 1 h and further tested in tension at RT.

Fig. 3. Orientation maps of the Al-3Mg-0.2Sc alloy subjected to 10 turns of HPT at either (a) 300 or (b) 450 K.

Fig. 4. Histograms of (a) the area fraction of grain diameters and (b) the misorientation angles of the Al-3Mg-0.2Sc alloy processed through 10 HPT turns at 300 or 450 K.

Fig. 5. TEM micrographs and corresponding SAED patterns revealing grains and dislocation structures in the Al-3Mg-0.2Sc alloy processed through 10 HPT turns at either (a, b) 300 or (c, d) 450 K.

Fig. 6. Orientation maps of the Al-3Mg-0.2Sc alloy subjected to 10 HPT turns at RT and subsequently annealed for 1 h at temperatures from 523 to 773 K.

Fig. 7. Orientation maps of the Al-3Mg-0.2Sc alloy subjected to 10 HPT turns at 450 K and subsequently annealed for 1 h at temperatures from 523 to 773 K.

Fig. 8. Average grain diameter as a function of annealing temperature for the Al-3Mg-0.2Sc alloy processed through 10 turns of HPT at 300 either or 450 K.

Fig. 9. (a, c) Bright and (b) dark field TEM and HRTEM images showing details of the (d) incoherent and (e, f) semi-coherent Al_3Sc precipitates of the Al-3Mg-0.2Sc alloy processed by up to 10 turns of HPT at RT and further annealed at 673 K for 1 h.

Fig. 10. (a, c, d and e) Bright and (b) dark field TEM images showing details of the Al_3Sc precipitates of the Al-3Mg-0.2Sc alloy processed by up to 10 turns of HPT at 450 K and further annealed at 673 K for 1 h.

Fig. 11. Histograms revealing the size distributions for the Al_3Sc precipitates in the Al-3Mg-0.2Sc alloy processed by up to 10 turns of HPT at either 300 or 450 K and further annealed at 673 K for 1 h.

Fig. 12. Plots of (a) yield strength as a function of $d^{-0.5}$ and (b) tensile strength as a function of elongation to failure for the Al-3Mg-0.2Sc alloy processed by HPT and further annealed for 1 h at temperatures ranging from 423 to 773 K.

Fig. 13. Schematic illustration of typical microstructural changes in an Al-Mg-Sc alloy after HPT processing at RT or 450 K followed by annealing at different temperatures.

Table captions:

Table 1. Crystallite size, microstrain and dislocation density for the Al-3Mg-0.2Sc alloy processed through 10 HPT revolutions at 300 or 450 K.

Table 2. Volume fraction of Al_3Sc particles (f), mean precipitate radius (r) and estimated Zener pinning pressure, P_z, for an Al-Mg-Sc alloy after heating at temperatures from 423 to 773 K for 1 h.

Table 3. Sum of the driving (P_d and P_g) and restraining (P_z) pressures for boundary migration (ΣP) and factor for boundary stability (ψ) for the Al-3Mg-0.2Sc alloy processed through 10 HPT turns at 300 or 450 K after annealing for 1 h at temperatures from 423 to 773 K.

Figures:

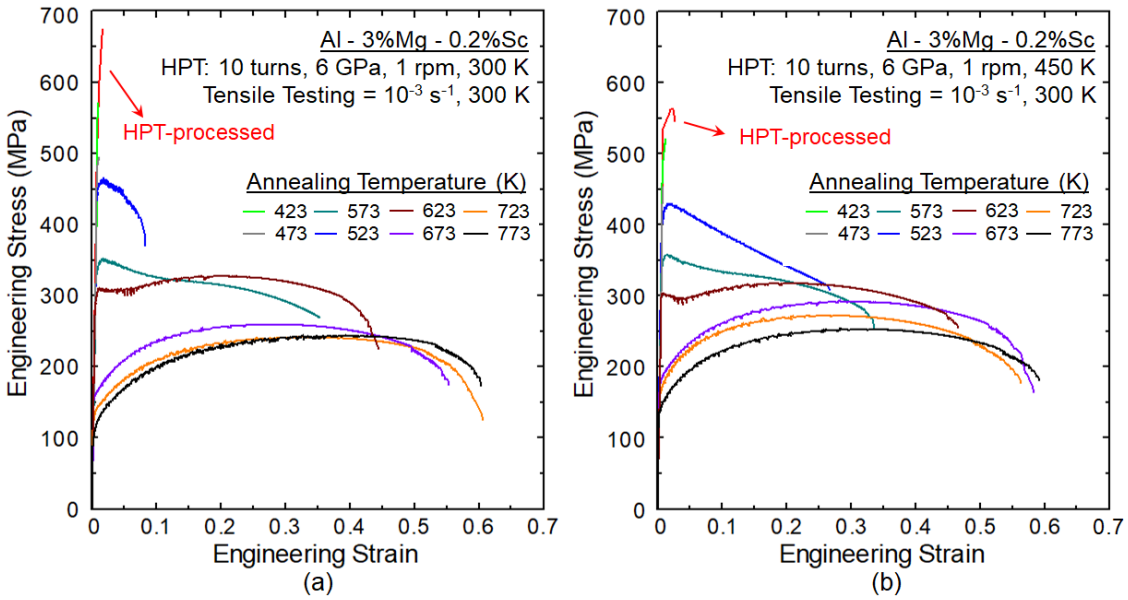

Fig. 1. Stress *vs* strain curves obtained at RT for the Al-3Mg-0.2Sc alloy processed by HPT at (a) 300 or (b) 450 K and annealed for 1 h at temperatures from 423 to 773 K.

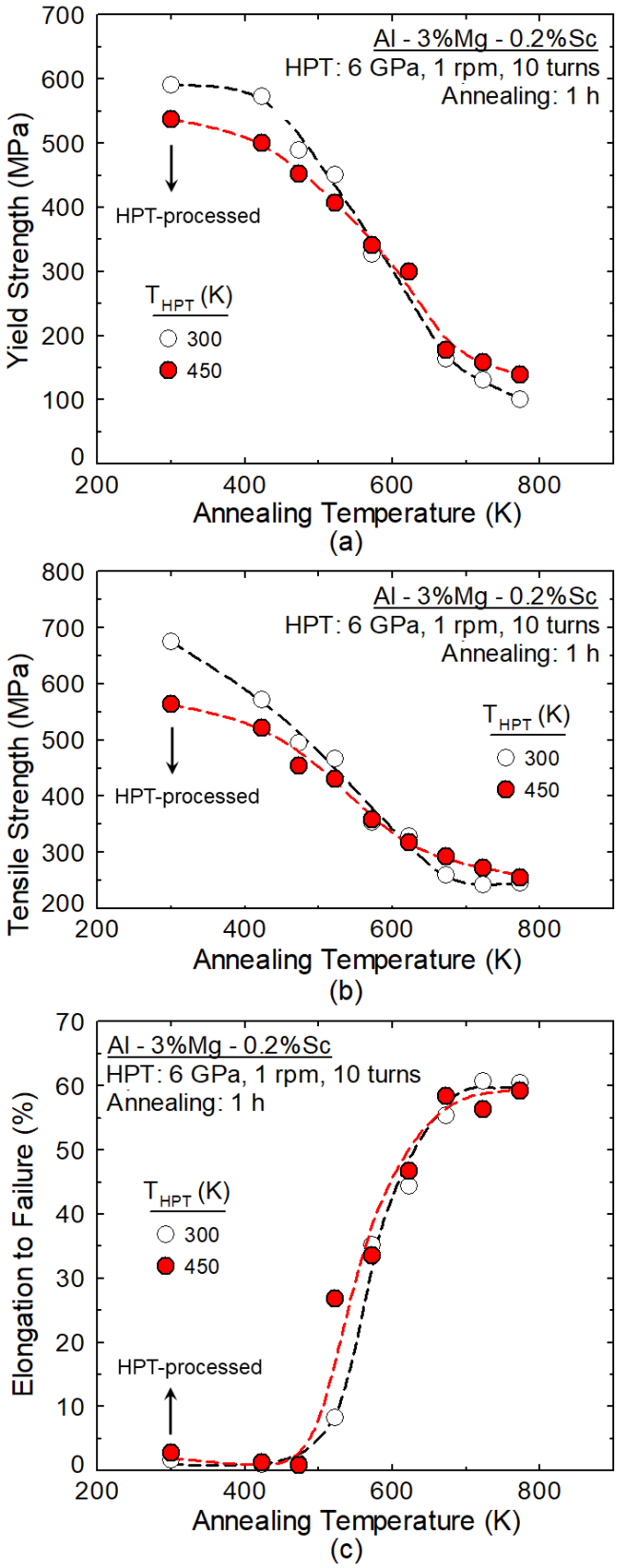

Fig. 2. (a) Yield stress, (b) tensile strength and (c) elongation to failure as function of annealing temperature for the Al-3Mg-0.2Sc alloy processed by HPT at (a) 300 or (b) 450 K, annealed for 1 h and further tested in tension at RT.

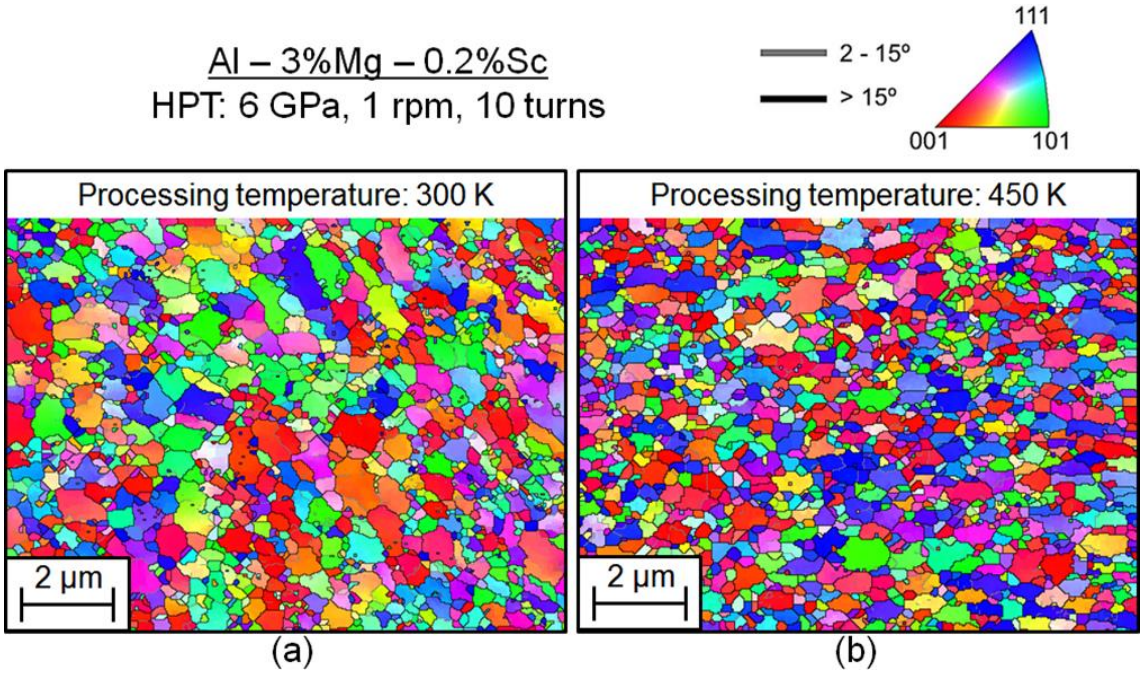

Fig. 3. Orientation maps of the Al-3Mg-0.2Sc alloy subjected to 10 turns of HPT at either (a) 300 or (b) 450 K.

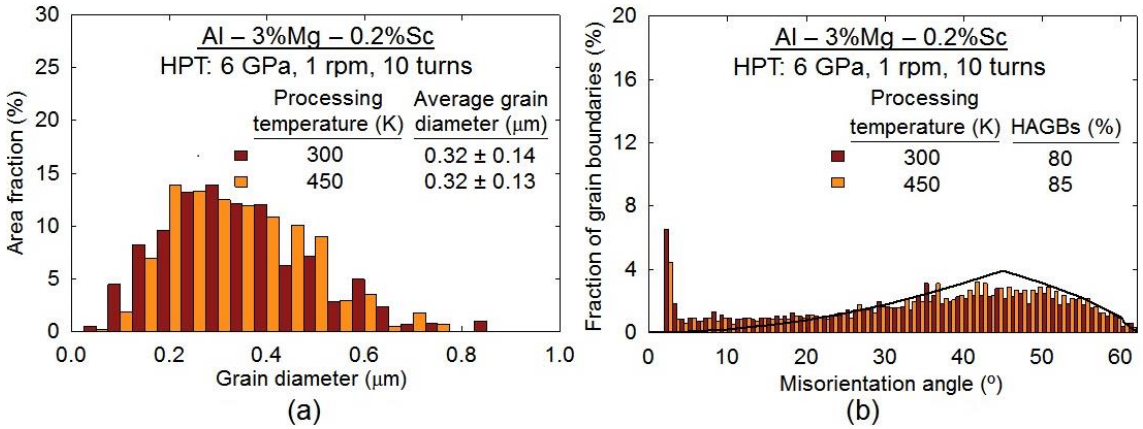

Fig. 4. Histograms of (a) the area fraction of grain diameters and (b) the misorientation angles of the Al-3Mg-0.2Sc alloy processed through 10 HPT turns at 300 or 450 K.

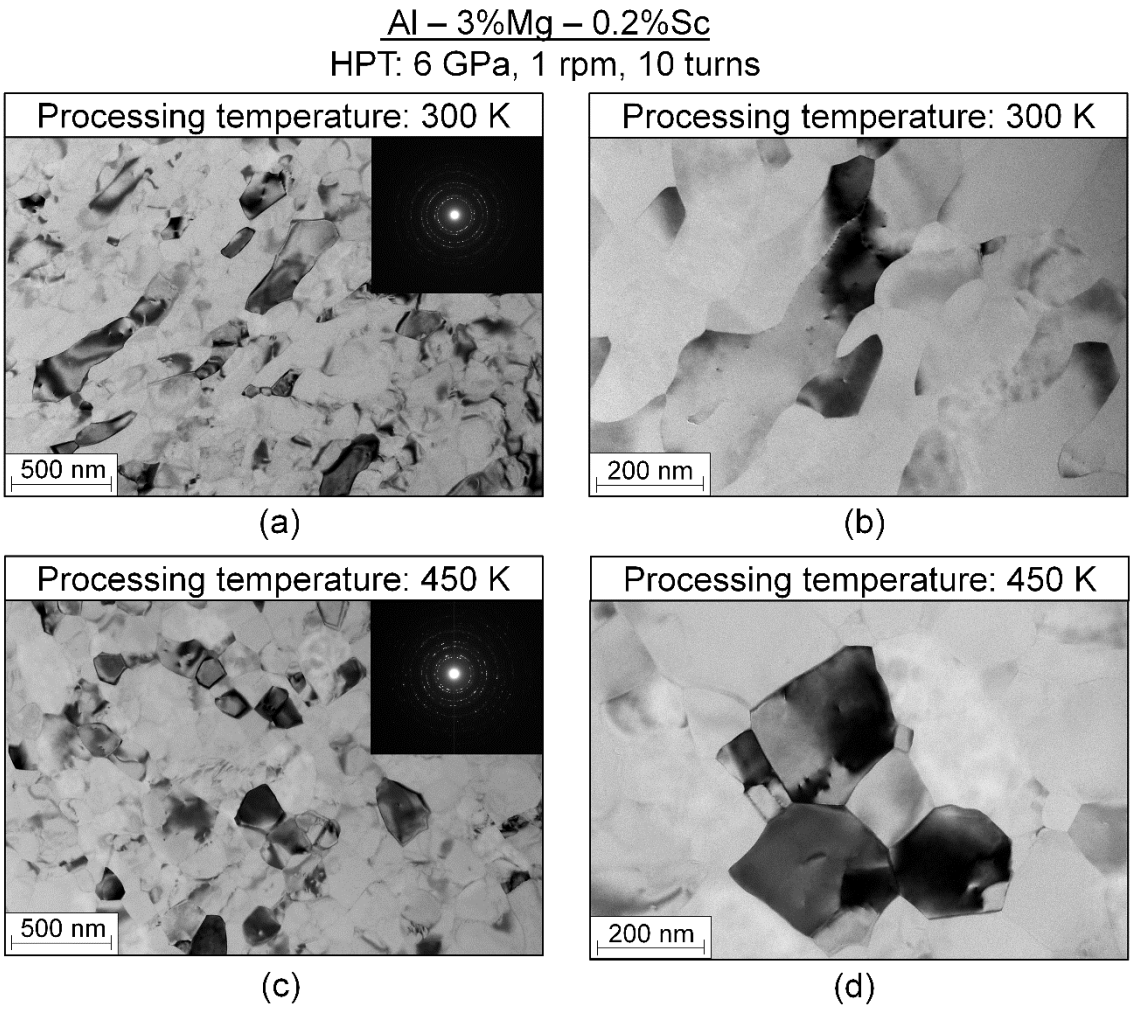

Fig. 5. TEM micrographs and corresponding SAED patterns revealing grains and dislocation structures in the Al-3Mg-0.2Sc alloy processed through 10 HPT turns at either (a, b) 300 or (c, d) 450 K.

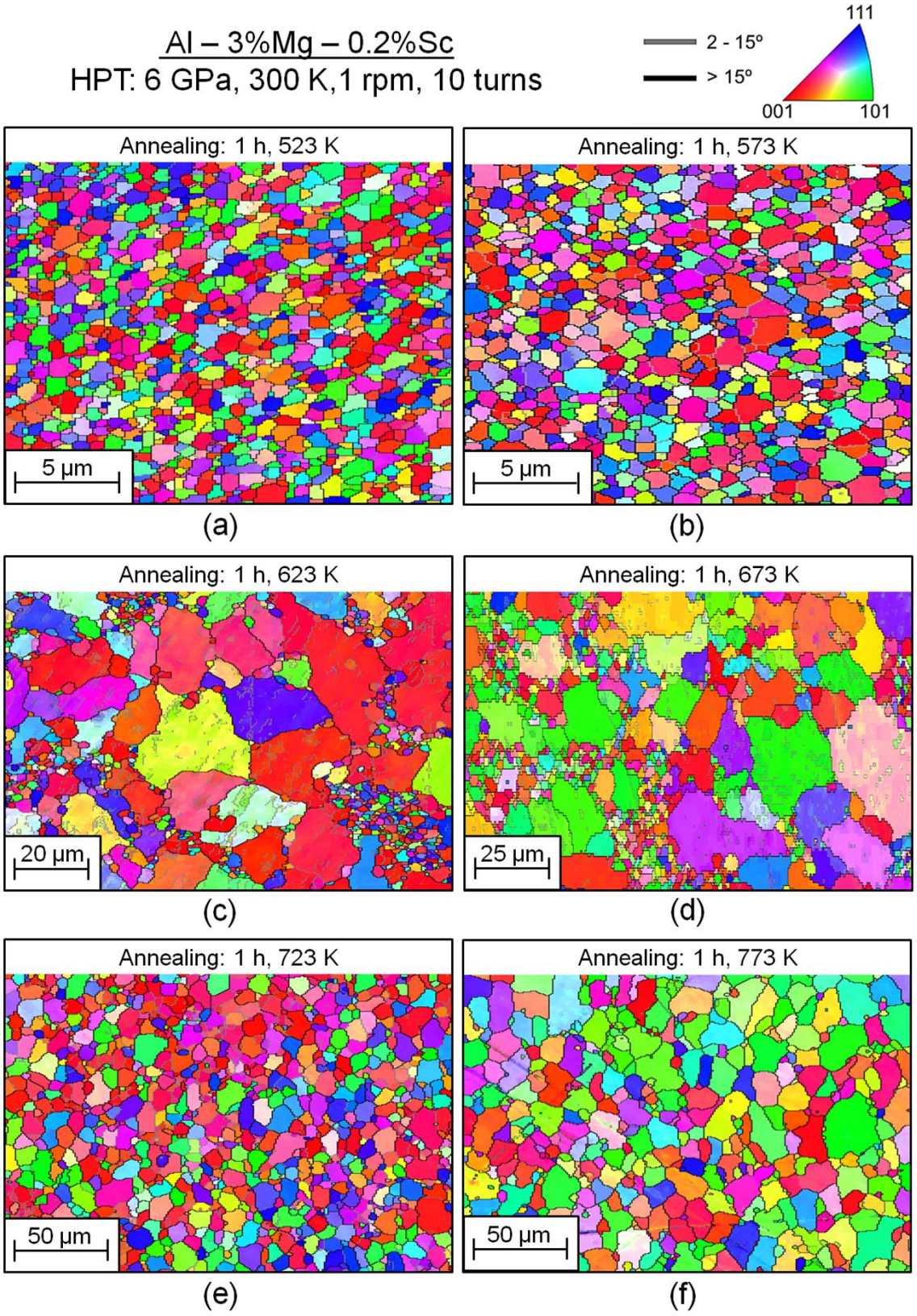

Fig. 6. Orientation maps of the Al-3Mg-0.2Sc alloy subjected to 10 HPT turns at RT and subsequently annealed for 1 h at temperatures from 523 to 773 K.

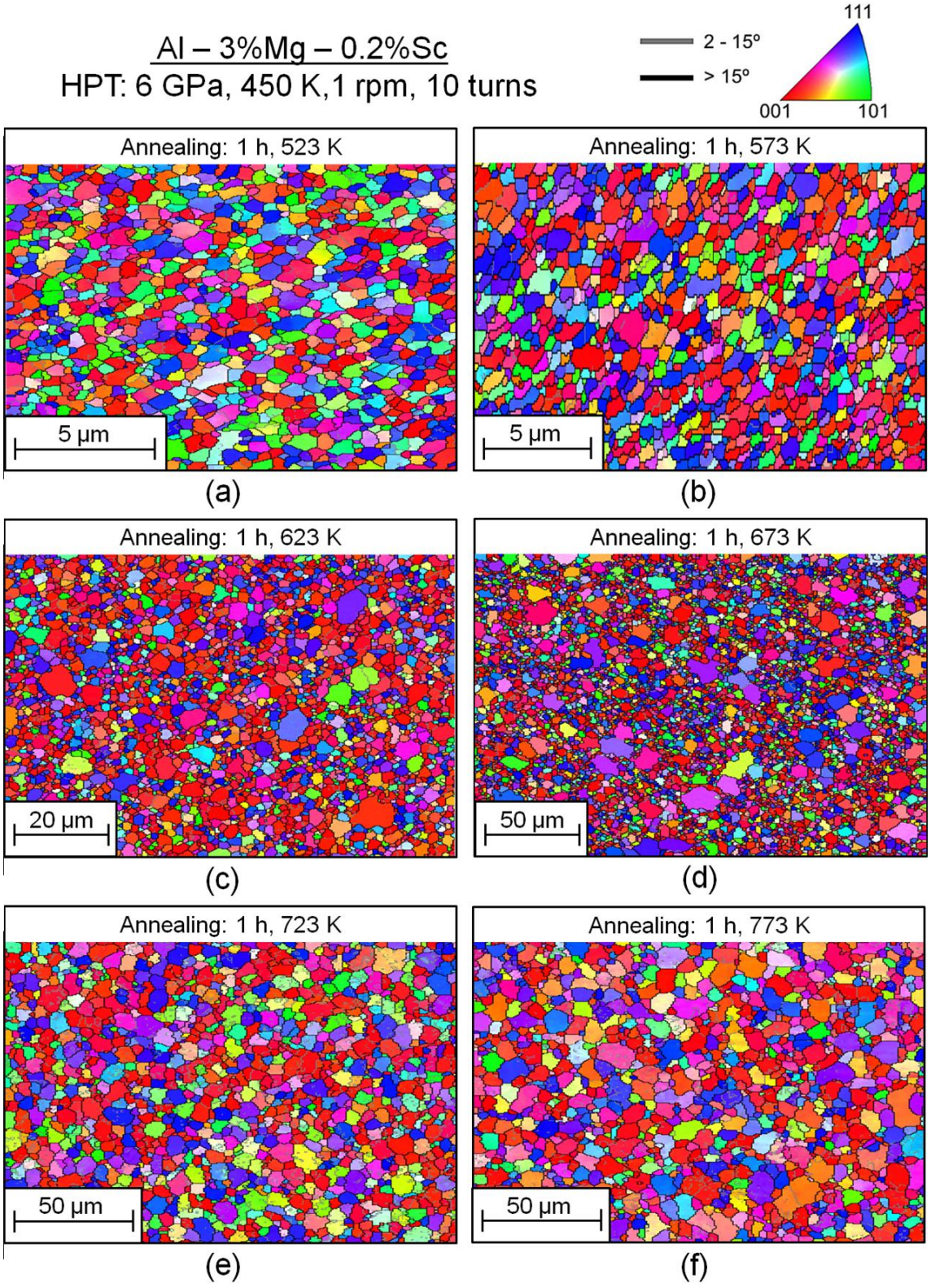

Fig. 7. Orientation maps of the Al-3Mg-0.2Sc alloy subjected to 10 HPT turns at 450 K and subsequently annealed for 1 h at temperatures from 523 to 773 K.

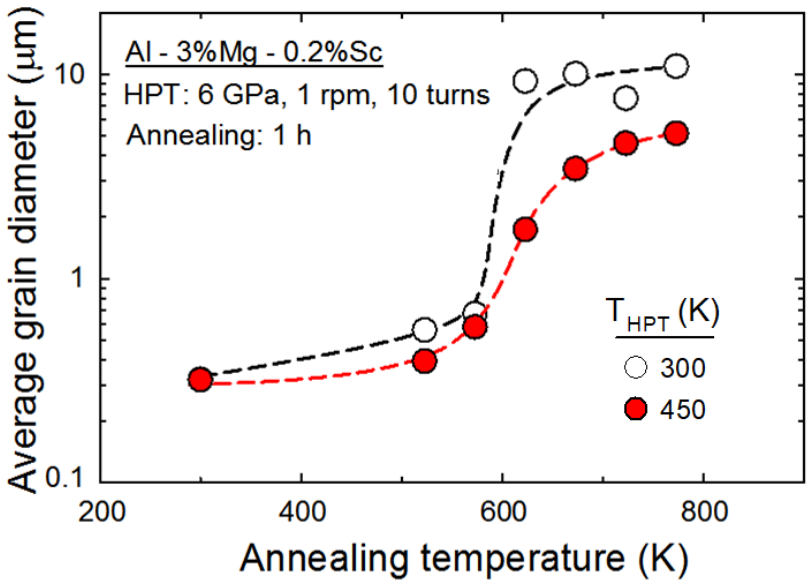

Fig. 8. Average grain diameter as a function of annealing temperature for the Al-3Mg-0.2Sc alloy processed through 10 turns of HPT at 300 either or 450 K.

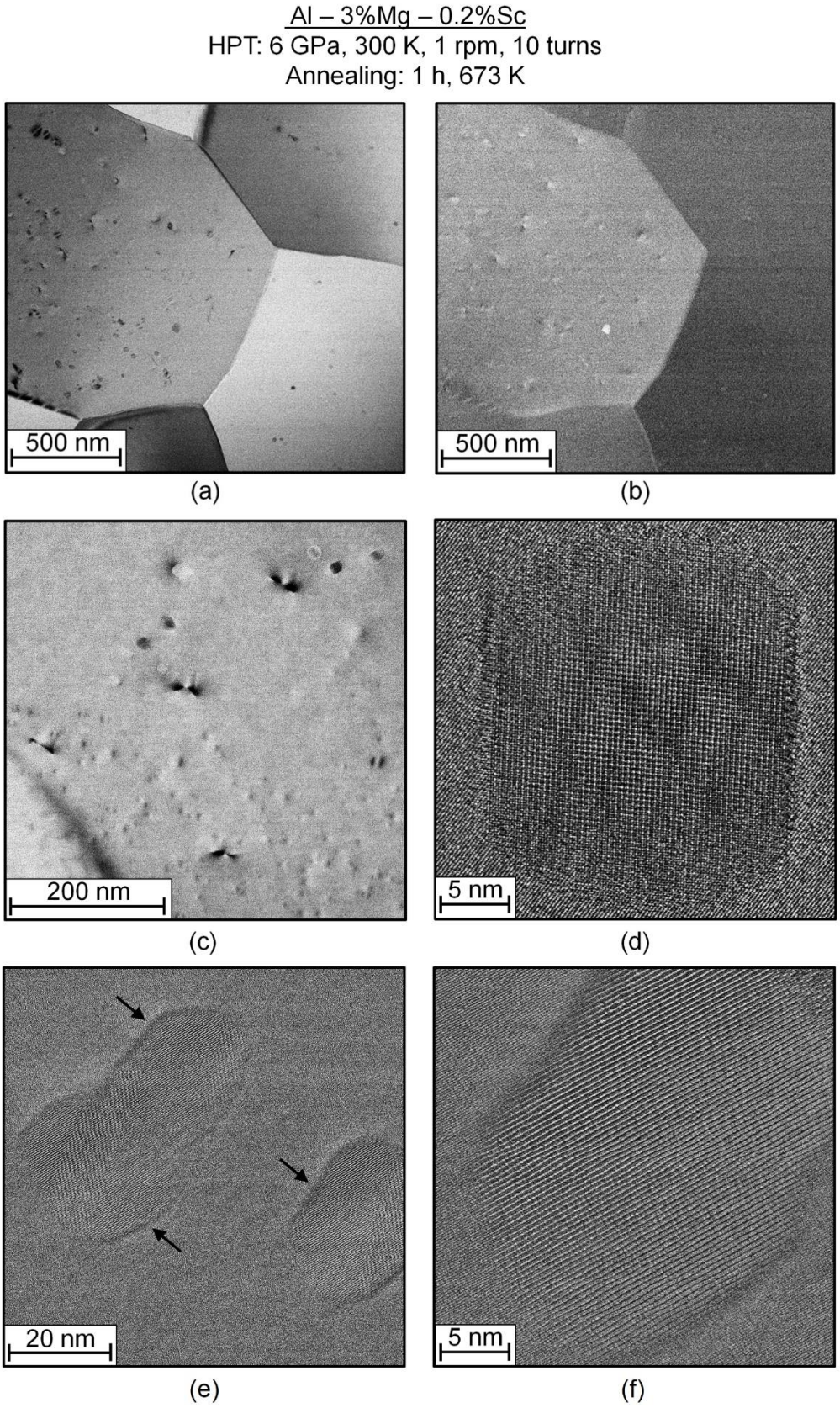

Fig. 9. (a, c) Bright and (b) dark field TEM and HRTEM images showing details of the (d) incoherent and (e, f) semi-coherent Al_3Sc precipitates of the Al-3Mg-0.2Sc alloy processed by up to 10 turns of HPT at RT and further annealed at 673 K for 1 h.

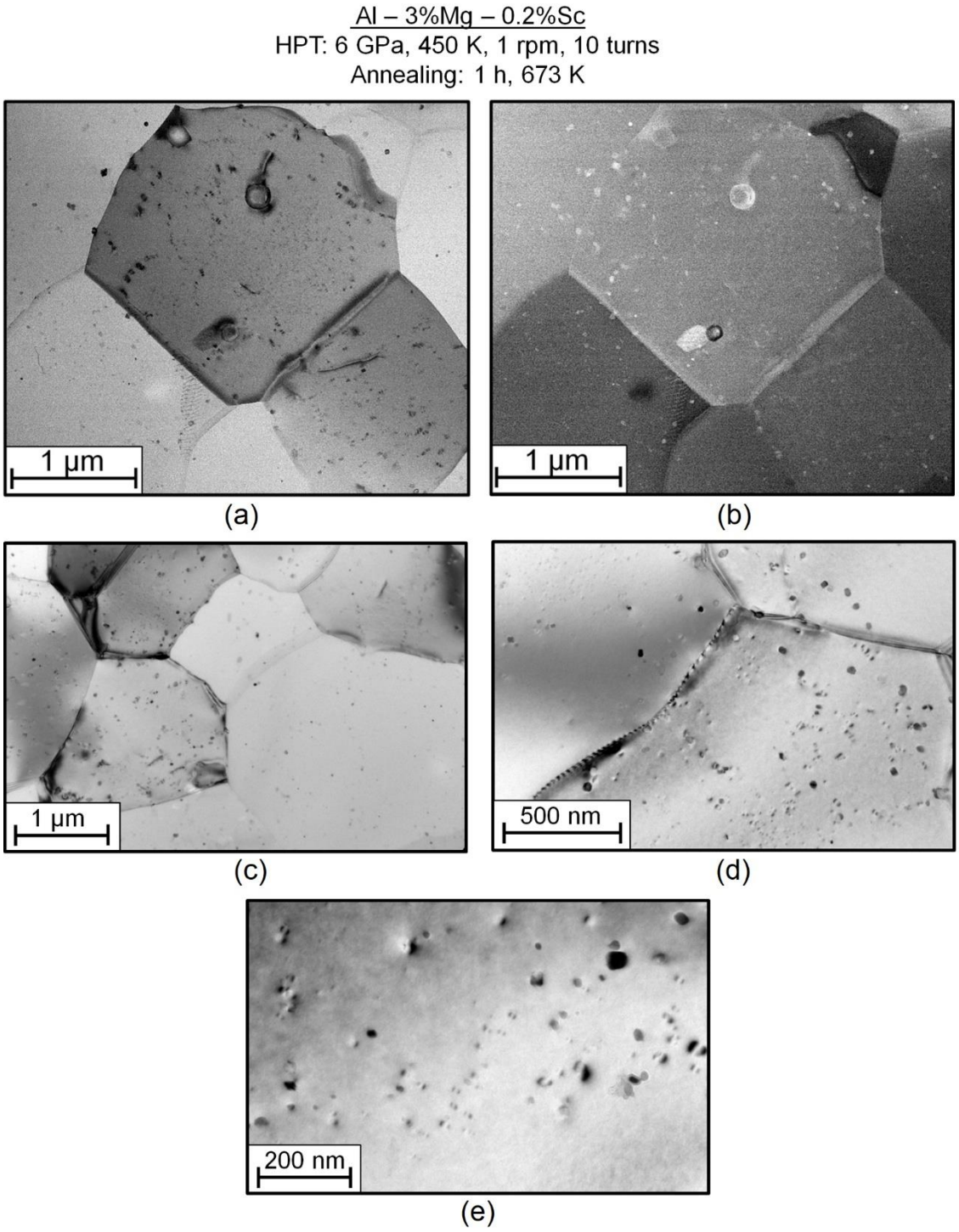

Fig. 10. (a, c, d and e) Bright and (b) dark field TEM images showing details of the Al_3Sc precipitates of the Al-3Mg-0.2Sc alloy processed by up to 10 turns of HPT at 450 K and further annealed at 673 K for 1 h.

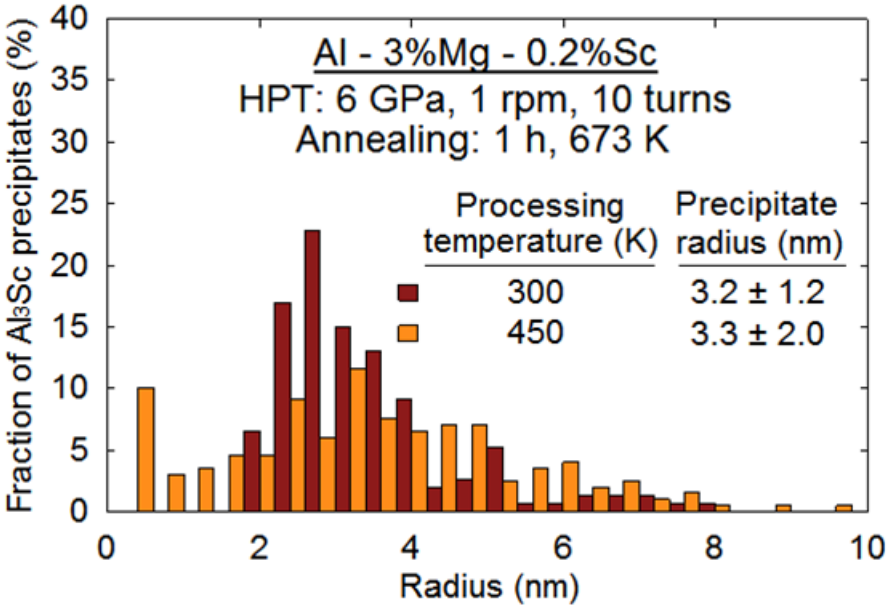

Fig. 11. Histograms revealing the size distributions for the Al_3Sc precipitates in the Al-3Mg-0.2Sc alloy processed by up to 10 turns of HPT at either 300 or 450 K and further annealed at 673 K for 1 h.

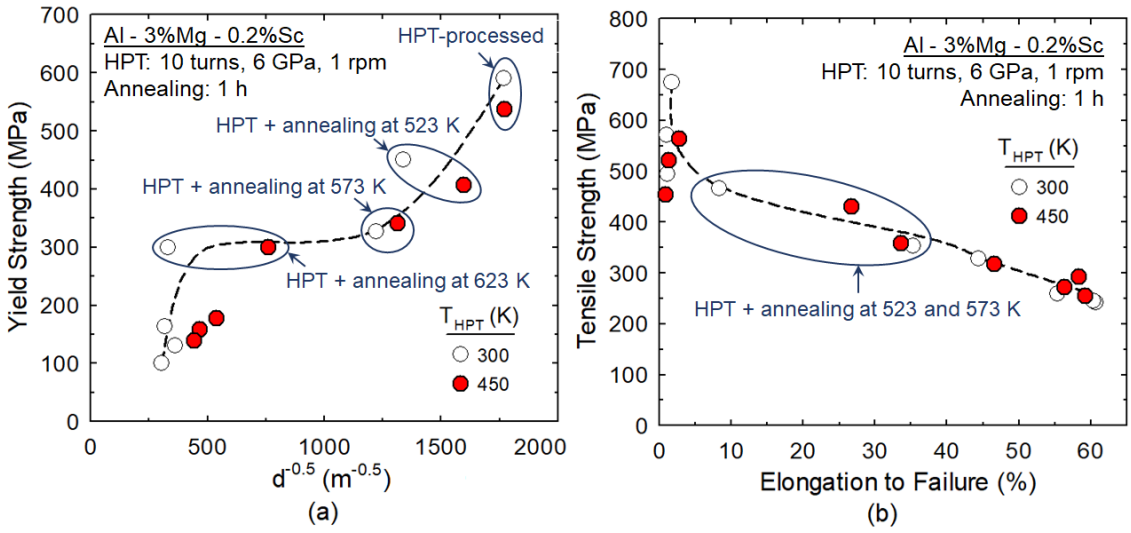

Fig. 12. Plots of (a) yield strength as a function of $d^{-0.5}$ and (b) tensile strength as a function of elongation to failure for the Al-3Mg-0.2Sc alloy processed by HPT and further annealed for 1 h at temperatures ranging from 423 to 773 K.

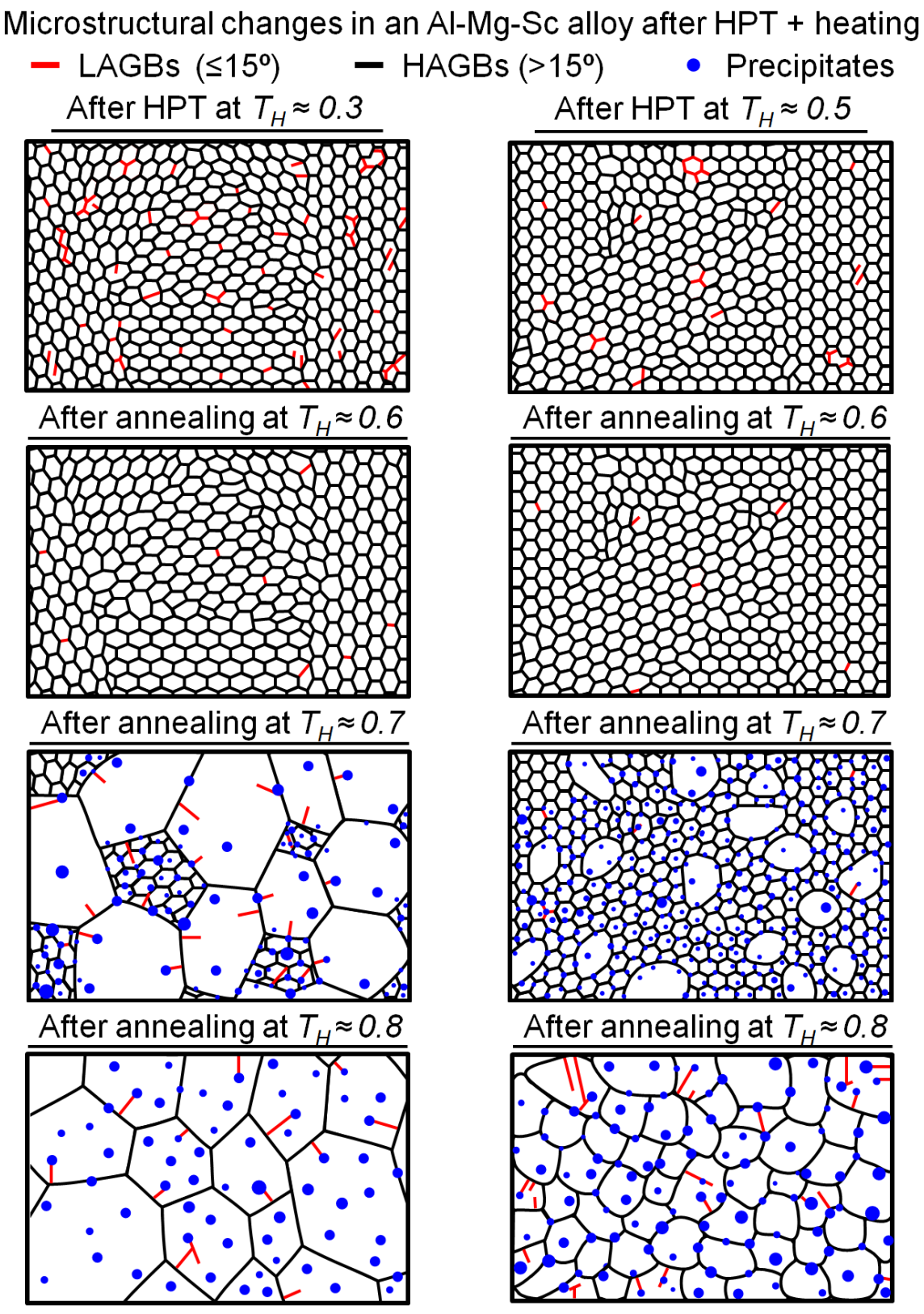

Fig. 13. Schematic illustration of typical microstructural changes in an Al-Mg-Sc alloy after HPT processing at RT or 450 K followed by annealing at different temperatures.

Table 1. Crystallite size, microstrain and dislocation density for the Al-3Mg-0.2Sc alloy processed through 10 HPT revolutions at 300 or 450 K.

Processing condition	*Crystallite size* (nm)	*Microstrain* (%)	*Dislocation density* ($m^{-2} \times 10^{13}$)
HPT: 300 K, 10 turns	160 ± 2	0.048 ± 0.004	3.6 ± 0.4
HPT: 450 K, 10 turns	190 ± 2	0.012 ± 0.002	0.7 ± 0.1

Table 2. Volume fraction of Al_3Sc particles (f), mean precipitate radius (r) and estimated Zener pinning pressure, P_z, for an Al-Mg-Sc alloy after heating at temperatures from 423 to 773 K for 1 h.

T (K)	f (%) [a]	r (nm)	P_z (MPa) [e]
573	0.50	1.0 [b]	2.43
623	0.48	1.8 [b]	1.29
673	0.46	3.2-3.3 [c] 3.5 [d]	0.70-0.68 0.64
723	0.43	9.5 [d]	0.26
773	0.33	21.5 [d]	0.08

[a] Calculated from the Al-Sc phase diagram assuming equilibrium conditions at temperature of annealing [7].
[b] Average radius of Al_3Sc precipitates in an Al-0.3Sc alloy aged for ~1 h [9].
[c] Values measured in the Al-3Mg-0.2Sc alloy in this research.
[d] Mean radius of Al_3Sc particles in an Al-0.25Sc alloy annealed for ~1 h [53].
[e] Calculated using Eq. 4 using $\gamma = 0.324$ Jm^{-2} [65].

Table 3. Sum of the driving (P_d and P_g) and restraining (P_z) pressures for boundary migration (ΣP) and factor for boundary stability (ψ) for the Al-3Mg-0.2Sc alloy processed through 10 HPT turns at 300 or 450 K after annealing for 1 h at temperatures from 423 to 773 K.

Processing condition	*T* (K)	P_d (MPa)	P_g (MPa)	ΣP (MPa)	ψ
HPT: 300 K, 10 turns	573	0.04	3.04	0.65	1.20
	623			1.79	0.64
	673			2.37	0.35
	723			2.86	0.11
	773			3.00	0.04
HPT: 450 K, 10 turns	573	0.01	3.04	0.62	1.20
	623			1.76	0.64
	673			2.36	0.34
	723			2.83	0.11
	773			2.97	0.04

Supplementary Material:

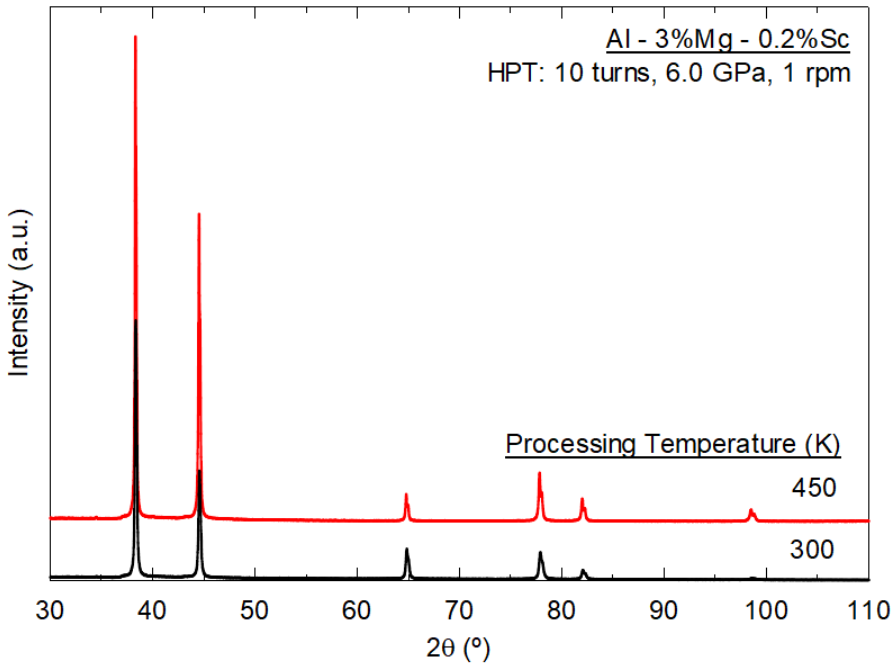

Fig. 1A. XRD profiles for the Al-3Mg-0.2Sc alloy processed through 10 revolutions of HPT at either (a) 300 or (b) 450 K.

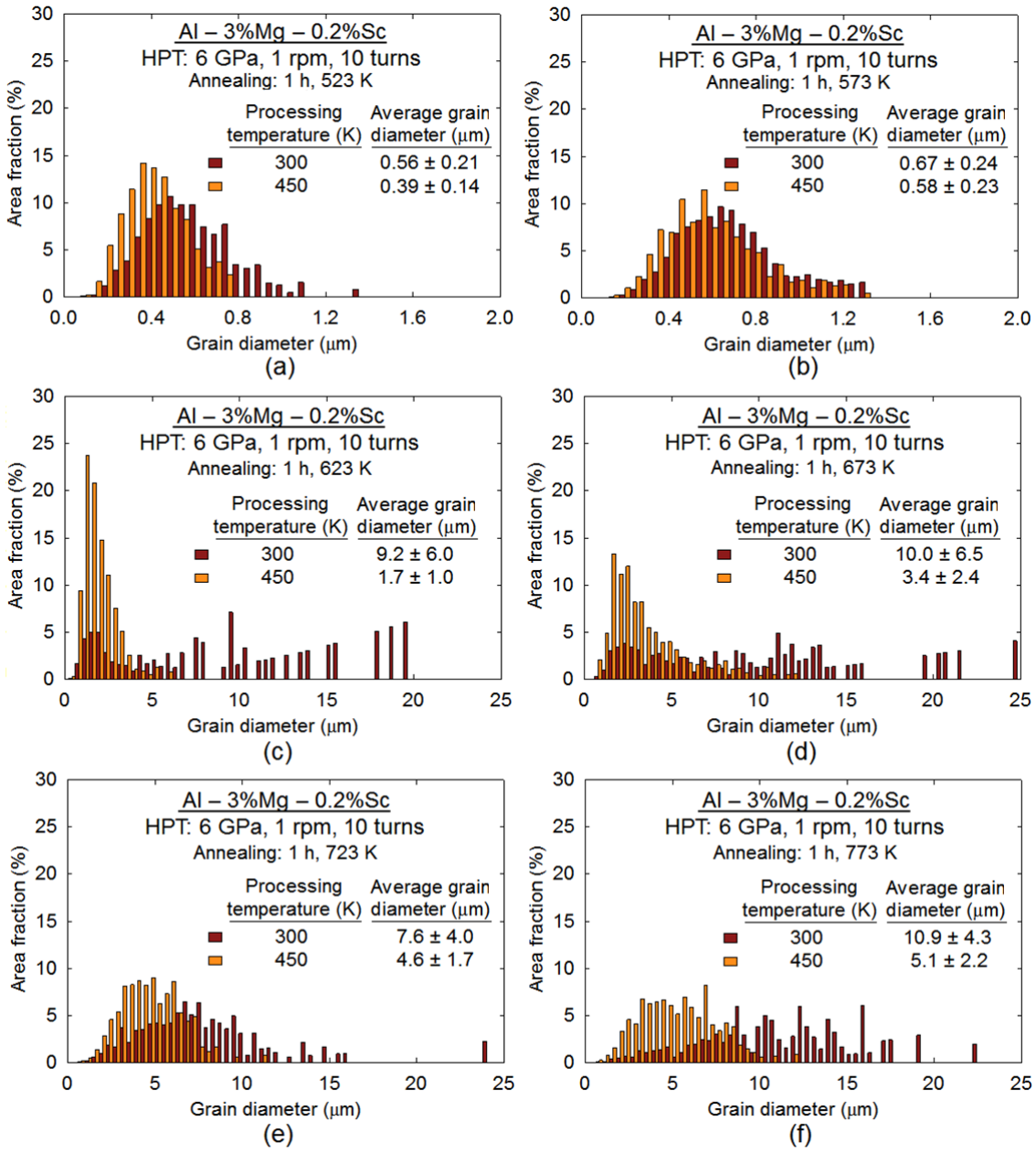

Fig. 2A. Histograms of the area fraction of grain diameters for the Al-3Mg-0.2Sc alloy processed by 10 HPT revolutions at 300 or 450 K and further annealed for 1 h at temperatures from 523 to 773 K.

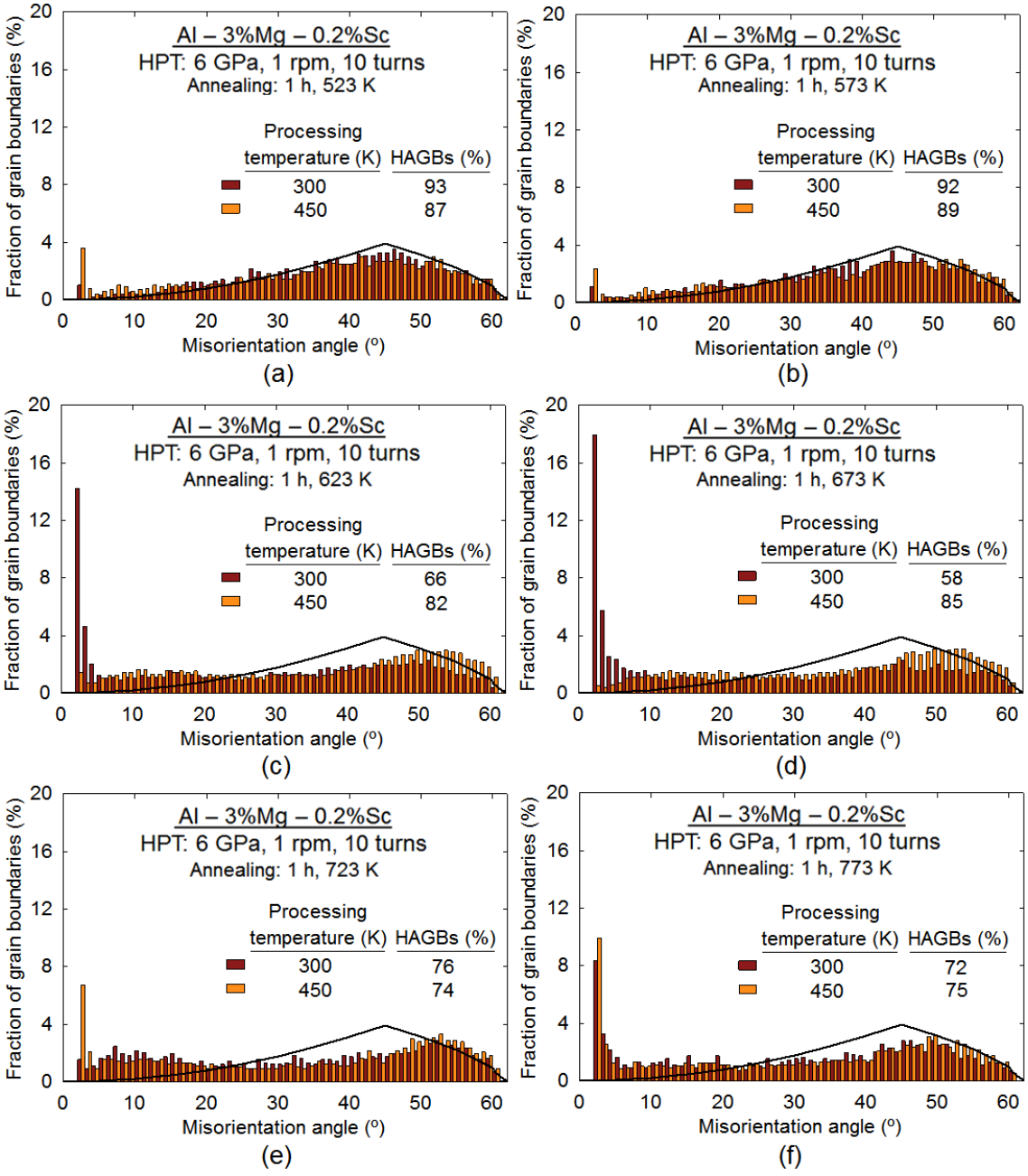

Fig. 3A. Histograms of fraction of grain boundaries as a function of misorientation angle for the Al-3Mg-0.2Sc alloy processed by 10 HPT revolutions at 300 or 450 K and further annealed for 1 h at temperatures from 523 to 773 K.